

# An organoid platform for ovarian cancer captures intra- and interpatient heterogeneity

Oded Kopper<sup>1,2</sup>, Chris J. de Witte<sup>3,15</sup>, Kadi Löhmußaar<sup>1,2,15</sup>, Jose Espejo Valle-Inclan<sup>3,15</sup>, Nizar Hami<sup>2,4</sup>, Lennart Kester<sup>1,2</sup>, Anjali Vanita Balgobind<sup>1,2</sup>, Jeroen Korving<sup>1,2</sup>, Natalie Proost<sup>5</sup>, Harry Begthel<sup>1,2</sup>, Lise M. van Wijk<sup>6</sup>, Sonia Aristín Revilla<sup>1,2</sup>, Rebecca Theeuwse<sup>5</sup>, Marieke van de Ven<sup>5</sup>, Markus J. van Roosmalen<sup>3</sup>, Bas Ponsioen<sup>2,4</sup>, Victor W. H. Ho<sup>7</sup>, Benjamin G. Neel<sup>7,8</sup>, Tjalling Bosse<sup>9</sup>, Katja N. Gaarenstroom<sup>10</sup>, Harry Vrieling<sup>6</sup>, Maaïke P. G. Vreeswijk<sup>6</sup>, Paul J. van Diest<sup>11</sup>, Petronella O. Witteveen<sup>12</sup>, Trudy Jonges<sup>11</sup>, Johannes L. Bos<sup>2,4</sup>, Alexander van Oudenaarden<sup>1,2</sup>, Ronald P. Zweemer<sup>13</sup>, Hugo J. G. Snippert<sup>2,4</sup>, Wigard P. Kloosterman<sup>1,2,14\*</sup> and Hans Clevers<sup>1,2,14\*</sup>

**Ovarian cancer (OC) is a heterogeneous disease usually diagnosed at a late stage. Experimental in vitro models that faithfully capture the hallmarks and tumor heterogeneity of OC are limited and hard to establish. We present a protocol that enables efficient derivation and long-term expansion of OC organoids. Utilizing this protocol, we have established 56 organoid lines from 32 patients, representing all main subtypes of OC. OC organoids recapitulate histological and genomic features of the pertinent lesion from which they were derived, illustrating intra- and interpatient heterogeneity, and can be genetically modified. We show that OC organoids can be used for drug-screening assays and capture different tumor subtype responses to the gold standard platinum-based chemotherapy, including acquisition of chemoresistance in recurrent disease. Finally, OC organoids can be xenografted, enabling in vivo drug-sensitivity assays. Taken together, this demonstrates their potential application for research and personalized medicine.**

Over the past decade, the field of epithelial ovarian cancer (OC) research has gone through a dramatic shift led by a series of recent discoveries<sup>1,2</sup>. It has become clear that OC is a heterogeneous disease consisting of a wide spectrum of distinct molecular and clinical entities. Epithelial ovarian neoplasms can be divided into three main groups: borderline tumors (BTs; non-carcinoma) and type I and type II tumors (carcinomas)<sup>3,4</sup>. BTs account for 15% of OC malignancies and consist primarily of serous BT (SBT) and mucinous BT (MBT) subtypes. BTs are frequently found adjacent to type I tumors and share many of their characteristics. It is therefore believed that they can transform into type I tumors<sup>3</sup>. Type I tumors are genetically stable and carry a distinct set of frequently mutated genes, including *KRAS*, *BRAF*, *PTEN* and *CTNNB1* (ref. 4). There are four main type I subtypes: low-grade serous (LGS), mucinous (MC), endometrioid (END) and clear cell (CCC) carcinomas<sup>4</sup>. Type II tumors comprise high-grade serous (HGS) tumors, which are the most common type of OC and account for 70–80% of mortalities<sup>2</sup>. HGS tumors frequently carry mutations in the *TP53* (96%), *BRCA1* and *BRCA2* genes (20%), and are an extreme example of chromosomally unstable cancer<sup>5,6</sup>. HGS tumors are believed to develop

either from the fimbria of the fallopian tube (FT)<sup>7</sup> or from the ovarian surface epithelium (OSE). However, the relative contribution of these tissues to tumor development is still under debate<sup>8</sup>.

Tumor cell lines and patient-derived tumor xenografts are the most commonly used human model systems for the study of OC<sup>9–13</sup>. Despite their contribution to cancer research, these models have a number of drawbacks<sup>14</sup>. Establishing a new cell line is a challenging and time-consuming process that involves a long period of fibroblast contamination reduction and has a low success rate. Thus, in many cases, the resulting cell lines are the product of a strong in vitro selection, which inevitably leads to the loss of tumor molecular characteristics, including copy number variations (CNVs), mutations and intrapatient heterogeneity<sup>15</sup>. In contrast to two-dimensional cell lines, xenografts reliably recapitulate components of the tumor environment, such as the three-dimensional structure and the interaction of cancer cells with stroma and blood vessel infiltration<sup>16</sup>. Nevertheless, xenografts involve significant investments in resources for their maintenance, are poorly suited for large-scale drug screening or for genetic manipulation, and undergo rapid mouse-specific tumor evolution<sup>17</sup>. To overcome these drawbacks

<sup>1</sup>Hubrecht Institute, Royal Netherlands Academy of Arts and Sciences and UMC Utrecht, Utrecht, the Netherlands. <sup>2</sup>Oncode Institute, Utrecht, the Netherlands. <sup>3</sup>Center for Molecular Medicine, University Medical Center Utrecht, Utrecht University, Utrecht, the Netherlands. <sup>4</sup>Molecular Cancer Research, Center for Molecular Medicine, University Medical Center Utrecht, Utrecht University, Utrecht, the Netherlands. <sup>5</sup>Preclinical Intervention Unit of the Mouse Clinic for Cancer and Ageing (MCCA) at the NKI, Amsterdam, the Netherlands. <sup>6</sup>Department of Human Genetics, Leiden University Medical Center, Leiden, the Netherlands. <sup>7</sup>Princess Margaret Cancer Center, University Health Network, Toronto, Ontario, Canada. <sup>8</sup>Perlmutter Cancer Center, NYU Langone Health, New York, NY, USA. <sup>9</sup>Department of Pathology, Leiden University Medical Center, Leiden, the Netherlands. <sup>10</sup>Department of Gynecology, Leiden University Medical Center, Leiden, the Netherlands. <sup>11</sup>Department of Pathology, University Medical Center Utrecht, Utrecht University, Utrecht, the Netherlands. <sup>12</sup>Department of Medical Oncology, Cancer Center, University Medical Center Utrecht, Utrecht University, Utrecht, the Netherlands. <sup>13</sup>Department of Gynaecological Oncology, Cancer Center, University Medical Center Utrecht, Utrecht University, Utrecht, the Netherlands. <sup>14</sup>The Netherlands Princess Máxima Center for Pediatric Oncology, Utrecht, the Netherlands. <sup>15</sup>These authors contributed equally: Chris J. De Witte, Kadi Löhmußaar, Jose Espejo Valle-Inclan \*e-mail: [w.kloosterman@umcutrecht.nl](mailto:w.kloosterman@umcutrecht.nl); [h.clevers@hubrecht.eu](mailto:h.clevers@hubrecht.eu)

and to allow personalized approaches to cancer treatment, novel OC research platforms are needed<sup>1,2,16</sup>.

As first shown for colorectal cancer<sup>18</sup>, tumor organoid cultures represent robust three-dimensional in vitro systems that faithfully recapitulate the tumor from which they are derived<sup>19–22</sup>. Organoid technology is based on the definition of a cocktail of growth factors and small molecules (used in conjunction with the basement membrane mimic Matrigel) to recreate the niche requirements for long-term growth of cells. Organoid cultures can be clonally established from single cells derived from tumor tissue, allowing the study of tumor heterogeneity<sup>23</sup>. Organoids allow rapid assaying of phenotype–genotype correlations and drug sensitivity, while recapitulating patient response<sup>22,24–26</sup>. The potential of organoid platforms for OC research was illustrated in a recent paper in which short-term cultured HGS organoids (7–10 d) were genomically characterized and then used in various assays to study DNA repair inhibitor response<sup>27</sup>.

Here we present and characterize an OC research platform that supports the efficient derivation and long-term expansion of OC organoids corresponding to non-malignant BTs, as well as MC, CCC, END, LGS and HGS carcinomas.

## Results

**Derivation of OC organoids.** OC tissue and blood were obtained from consenting patients who underwent tumor resection and/or drainage of ascites/pleural effusion, either before or after (neoadjuvant) chemotherapy (Supplementary Table 1). For each cancer case, the available tissue was used for organoid derivation, DNA isolation and histological analysis. Tumor pieces designated for organoid derivation, were further dissociated and the isolated tumor cells were suspended in basement membrane extract (BME), plated and supplemented with medium (Extended Data Fig. 1a).

We used a recently described FT organoid medium<sup>28</sup> as our starting point for OC medium optimization. To improve organoid derivation rate, compounds that follow two main guiding criteria were tested as additives to the FT baseline medium: (1) compounds previously reported to be highly expressed in ovarian tumors and therefore hypothesized to support OC growth<sup>29,30</sup> and (2) factors used to support OC cell growth<sup>31,32</sup> and other types of tumor organoids<sup>21,25</sup>. We noted that addition of hydrocortisone, forskolin and heregulin $\beta$ -1 to FT medium improved the efficiency of OC organoid derivation. We also observed that Wnt-conditioned medium, an essential component of the FT medium, was not essential for all tumor organoid lines. Moreover, it had a negative effect on some of the lines, presumably due to the presence of serum in the conditioned medium and not Wnt itself. Therefore, we used two types of OC medium for organoid derivation: with ('OCwnt medium') or without ('OC medium') Wnt-conditioned medium (Supplementary Table 2). Typically, it became obvious after two to three passages which of the two media was optimal for individual OC cultures. OC organoid growth rates showed significant variability between cases, with passaging intervals varying from one to four weeks and split ratios ranging from 1:1.5 to 1:4 (Supplementary Table 3). Organoids could be expanded long term, that is, at the time of final submission, 22 lines had been passaged more than 15 times and 4 lines more than 30 times without slowing down (Extended Data Fig. 2 and Supplementary Table 3). Organoids could be cryopreserved and efficiently recovered (85% success rate,  $n=33$ ; Supplementary Table 3).

OC is often diagnosed after the tumor has already metastasized. In some cases, we were able to obtain both the primary tumor and the different metastatic lesions. We were therefore able to derive multiple organoid lines from individual patients. In one case, we established primary and recurrent tumor organoids from the same patient. In total, we established 56 organoid lines, derived from 32 different patients. Organoids were derived with a success rate of 65%, representing both pre-malignant and malignant neoplasms

covering the spectrum of OC, including MBT, SBT, MC, LGS, CCC, END and HGS (Fig. 1a and Supplementary Table 4). OC organoid nomenclature is based on their histopathological subtype and a number that refers to patient and tumor location. Patient clinical data are presented in Supplementary Table 1.

**Derivation of normal FT and OSE organoids from BRCA germline mutation carriers.** Women with germline mutations in the *BRCA1/BRCA2* genes are at high risk of developing OC<sup>33,34</sup>. Therefore, organoids from normal FT and OSE of these individuals, in addition to non-carriers, should provide a valuable resource for research on the early stages of tumor development. We obtained FT and ovarian tissue from women undergoing prophylactic bilateral salpingo-oophorectomy (pBSO). As previously reported for FT organoids<sup>28</sup>, pBSO-derived FT organoids were visible within 3–4 d after isolation, displayed a rounded, cystic phenotype and could be maintained long term. Consistent with their tissue of origin, FT organoids expressed markers of both secretory and ciliated cells (PAX8 and acetylated- $\alpha$ -tubulin, respectively), and contained beating ciliated cells (Extended Data Fig. 3a–c and Supplementary Video 1).

OSE organoids displayed a slower growth rate compared with FT organoids. They were usually visible 1–2 weeks after plating and could be passaged once every 2–3 weeks for extended periods of time. OSE organoids displayed a cystic phenotype and expressed cytokeratin 8, demonstrating their epithelial origin (Extended Data Fig. 3d).

In total, we were able to derive (success rate >90%) FT organoids from ten pBSO-patients and OSE organoids from six pBSO-patients. In addition, we derived two FT lines from non-carriers. Normal organoid nomenclature and patient information data for each line are presented in Supplementary Table 5.

**Morphological and histological characterization of OC organoids.** Normal FT and OSE organoid lines consistently displayed a cystic morphology with some epithelium folds and invaginations, which appeared on organoid maturation (Extended Data Fig. 3). In contrast, OC organoids showed wide morphological variation between and within distinct histological subtype groups (Extended Data Fig. 1b,c). Most BT organoids were cystic, whereas MC, LGS, END and CCC organoids formed denser organoid structures harboring multiple lumens. HGS organoids presented a wide morphological spectrum, varying from cystic to dense with different degrees of circularity and cellular cohesiveness (Extended Data Fig. 1c,d). Scanning electron microscopy (SEM) revealed that morphological heterogeneity was not restricted to organoid shape, but also occurred at the cellular level (Extended Data Fig. 1c). Moreover, SEM showed different degrees of cellular organization, as evidenced by cellular cohesiveness and microvilli alignment.

To compare organoids to their corresponding tumor tissue, we performed hematoxylin and eosin (H&E) staining and evaluated expression of OC protein biomarkers, such as paired box gene 8 (PAX8) and tumor protein p53. Of note, the tumor organoids consist of the transformed epithelial cells of a tumor, but do not contain immune, vessel or connective tissue elements. Histological analysis of the primary tumor tissue used for organoid derivation revealed different degrees of normal cell contamination as indicated by H&E and p53 staining (Extended Data Fig. 2c). This stressed the need for histological analysis of the primary tissue used for organoid derivation, as low tumor purity can influence organoid derivation efficiency and genomic correlation between organoids and tissue.

H&E staining of OC organoids revealed multiple tumor characteristics, such as the presence of papillary-like structures, nuclear and cellular atypia, and features of hobnail cells (Fig. 1 and Extended Data Fig. 1d). These characteristics were not detected in normal FT and OSE organoids, which, in contrast, displayed

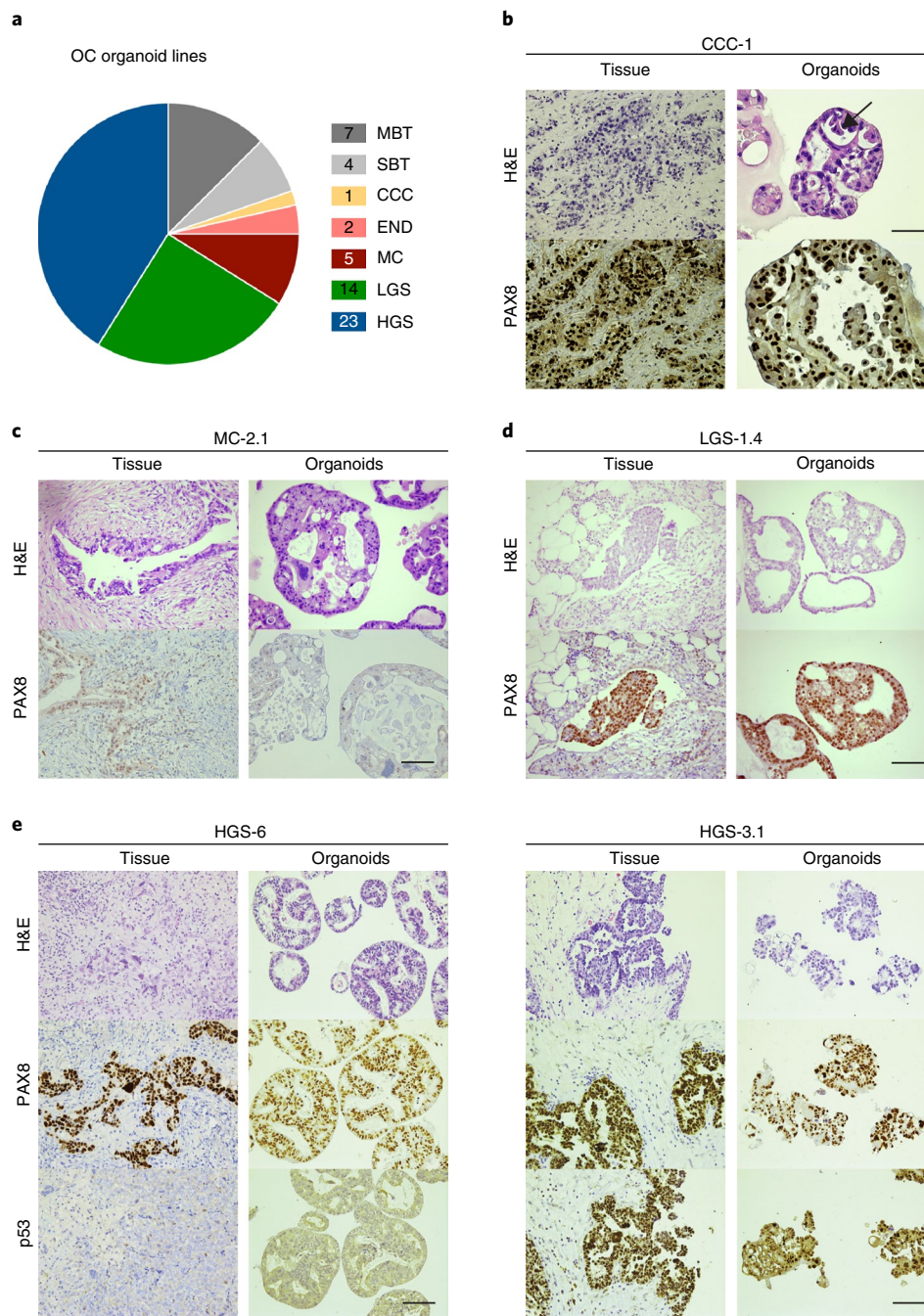


**Fig. 1 | Subtype diversity and histological characterization of OC organoids.** **a**, An overview of established OC organoid lines according to their subtype distribution. Numbers in the legend represent the number of lines established from each subtype. **b**, Histological comparison of CCC organoids and their corresponding tumor tissue. Top and bottom panels show H&E and PAX8 staining, respectively. Arrow indicates hobnail cells, which characterize CCC. Scale bar, 100  $\mu$ m. **c**, Histological comparison of representative MC organoids and their corresponding tumor tissue. Top and bottom panels show H&E and PAX8 staining, respectively. Tumor and organoids were negatively stained for PAX8, a marker of the serous subtype. Scale bar, 100  $\mu$ m. **d**, Histological comparison of representative LGS organoids and their corresponding tumor tissue. Top and bottom panels show H&E and PAX8 staining, respectively. Organoids maintain positive PAX8 staining. Scale bar, 100  $\mu$ m. **e**, Histological comparison of HGS organoids and their corresponding tumors (HGS-6 on the left and HGS-3.1 on the right). H&E staining of the HGS-6 organoid line showed papillary-like structures growing into the lumen, forming a dense phenotype. HGS-3.1 organoids are characterized with disorganized morphology, which is evident by loss of organoid circularity and cellular cohesiveness. PAX8 positively stains both organoids and the tumor cells within the tissue. Mutations in the *TP53* gene can lead to protein loss, as presented by the HGS-6 organoid/tumor pair, or strong nuclear staining, presented by the HGS-3.1 organoid/tumor pair. Histological characterization across the different organoid lines is presented in Extended Data Fig. 2e and Supplementary Table 6. Scale bar, 100  $\mu$ m.

well-organized epithelium (Extended Data Fig. 3). Moreover, in an H&E-based blinded test conducted by a certified pathologist on samples from normal FT and OSE organoids ( $n=5$ ) as well

as OC organoids ( $n=18$ ), only FT and OSE organoids were classified as ‘normal’. OC organoids were either classified as ‘non-definitive’ ( $n=5$ , 28%) or malignant ( $n=13$ , 72%). OC organoids

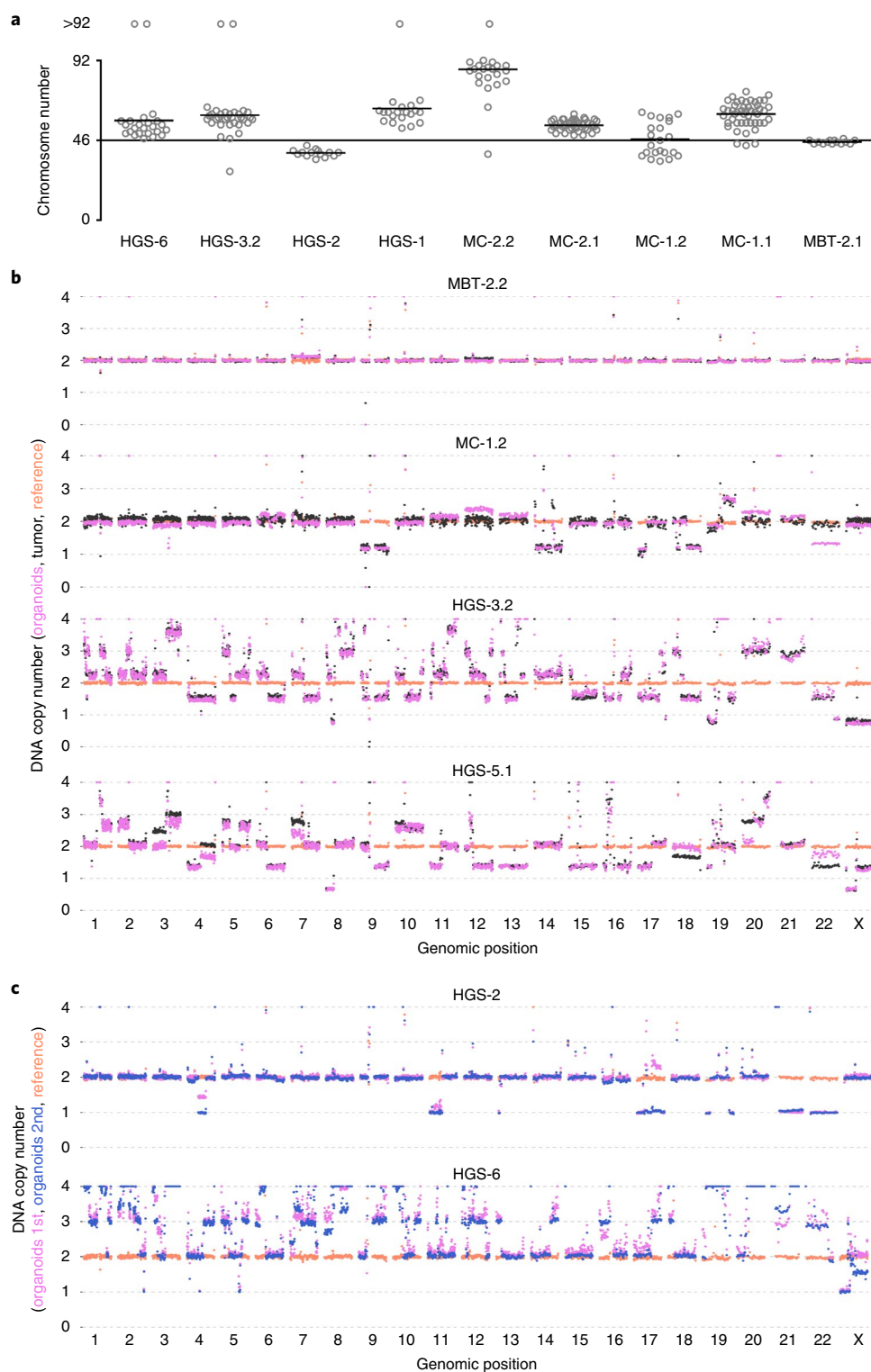


**Fig. 2 | Organoids maintain genomic landscape of corresponding tumors.** **a**, Scatter plot presenting chromosome number distribution and mean, based on organoid metaphase spreads. All the lines display aneuploidy except for the BT sample (MBT-2.1). Some of the organoid lines present a relatively narrow chromosome number distribution (MBT-2.1, MC-2.1, HGS-2), whereas others show a wide distribution (MC-1.1, MC-1.2), an indication of tumor heterogeneity. Differences between organoid lines that were derived from a single patient (MC-1.1/MC-1.2 and MC-2.1/MC-2.2) implies intrapatient heterogeneity.  $n$  = number of analyzed metaphase spread, from left to right: 24, 33, 14, 20, 24, 40, 22, 48 and 14. **b**, Genome-wide CNV analysis of tumor and organoid pairs. For each sample, CNV profile of blood germline reference (orange), tumor (black) and organoids (pink) are displayed. CNVs observed in original tumor samples are maintained in organoid lines. MBT-2.2 organoid line displays a relatively flat CNV pattern in accordance with MBT-2.1 that was derived from the same patient and shows normal metaphase spreads (in Fig. 2a). HGS lines display extreme CNV abnormalities (see also Extended Data Fig. 4). **c**, Genome-wide CNV analysis of early (organoids 1st) and late (organoids 2nd) passage organoid pairs (HGS-2, passage 6 versus passage 15; HGS-6, passage 8 versus passage 21). A ploidy of 3 was assumed for this sample. For each sample, CNV profile of blood germline reference (orange), early (pink) and late (blue) passaged organoid are displayed. CNV profiles observed in organoid samples are maintained.

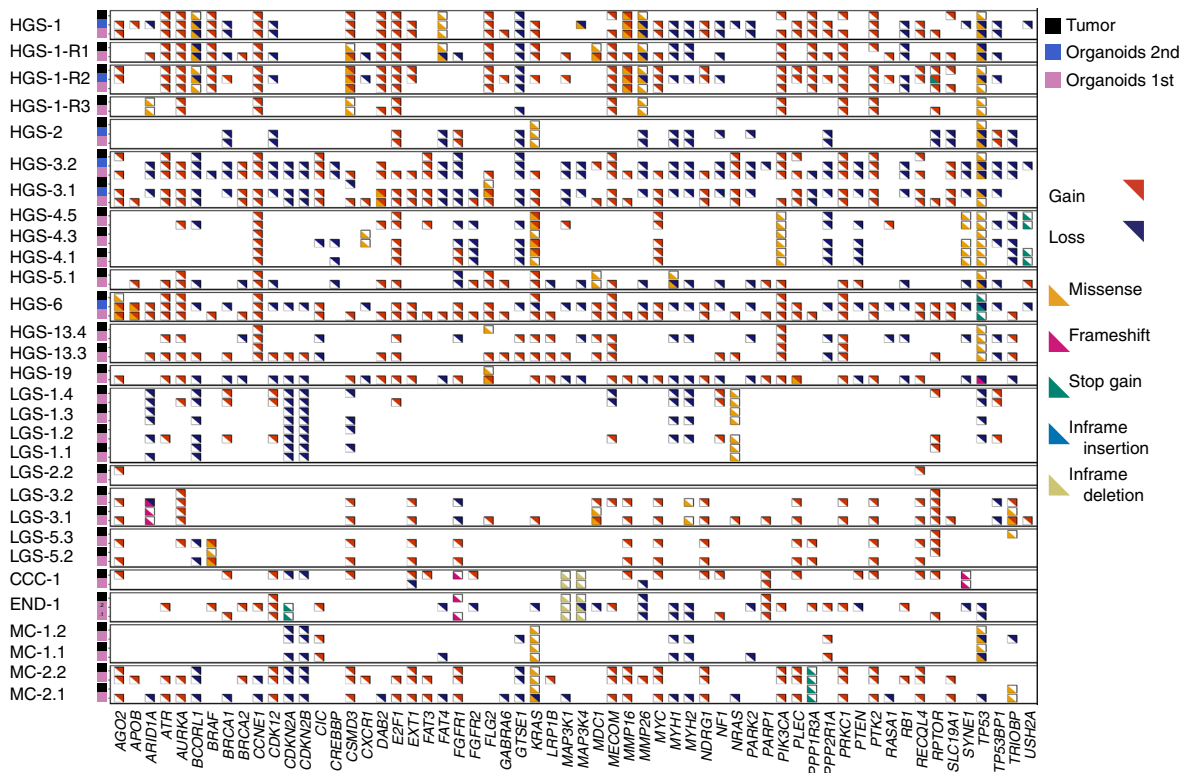


**Fig. 3 | Somatic mutations and amplifications/deletions in OC organoids.** Somatic mutations and amplifications/deletions in relevant genes of ovarian cancer. For each sample, tumor/organoid pairs are displayed and indicated by color coding (black, tumors; pink, organoids; blue, organoids re-sequenced and analyzed after extended passaging). Passage number at which organoid lines were sequenced is given in Supplementary Table 7.

that were classified as ‘non-definitive’ corresponded to BT and LGS tumors ( $n=4$  and  $n=1$ , respectively). In agreement with their histological classification, most MBT and MC organoid lines were positive for periodic acid–Schiff (9 out of 11) and negative for PAX8 (7 out of 11) staining, the latter a hallmark that distinguishes ovarian mucinous and serous tumors (Fig. 1c and Supplementary Table 6)<sup>35</sup>. Ovarian serous organoids that were tested retained PAX8 and p53 expression status as observed for their corresponding tumor tissue (Fig. 1d,e, Extended Data Fig. 2e and Supplementary Table 6). Mutations in the *TP53* gene can lead to diverse patterns of p53 staining, such as protein loss or strong nuclear staining. Such patterns were observed in different HGS organoid lines and their corresponding tumor tissue and were in agreement with their sequencing data (Fig. 1e and Supplementary Table 7). Organoids displayed a high percentage of Ki67-positive cells (Extended Data Fig. 2b). Thus, histological analysis of OC organoids demonstrated their similarity to the carcinoma fields within the corresponding primary tumors and their distinction from non-malignant FT and OSE organoids.

**Organoids faithfully recapitulate OC at the genomic level.** To further validate that OC organoids are composed of malignant cells, we performed metaphase spread analysis. The majority of tested organoid lines were aneuploid, a well-characterized hallmark of most solid tumors<sup>36</sup>. Interestingly, in some cases, a significant variation in average chromosome number was observed for different organoid lines derived from the same patient (Fig. 2a).

To determine whether OC organoids faithfully recapitulate the genomic landscape of the primary tumors from which they were derived, we next performed whole-genome sequencing (WGS) analysis. In total, we sequenced 40 organoid lines from 22 different patients. The corresponding tumor and normal blood samples

for 35 of these lines were also sequenced and used as a reference (Supplementary Table 7). We first used WGS data to estimate the percentage of malignant cells in both organoid and tumor samples<sup>37</sup>. As predicted from histological analysis, in most cases, cancer cell content of organoids was considerably higher than that of the corresponding tumor (tumor organoids  $88.1 \pm 23\%$  versus tumor tissue  $45.1 \pm 9.2\%$  (mean  $\pm$  s.d.) across all samples; Extended Data Fig. 2d and Supplementary Table 7). CNV analysis revealed similar patterns between organoid/tumor pairs (Fig. 2b and Extended Data Fig. 4a). Moreover, comparing the genomic landscape from early and late passage HGS organoids revealed that CNVs were well maintained even after prolonged passaging (HGS-1, passage 8 versus 32; HGS-2, passage 6 versus 15; HGS-3.1, passage 4 versus 32; HGS-3.2, passage 4 versus 25; HGS-6, passage 8 versus 21; HGS-1-R2, passage 4 versus 17; Fig. 2c and Extended Data Fig. 4a). Most organoids derived from HGS tumors displayed many CNVs, whereas organoids derived from type I tumors and BTs revealed a relatively subtle number of CNVs (Fig. 2b and Extended Data Fig. 4a). Thus, OC organoids recapitulate the genomic characteristics of the different OC subtypes from which they are derived<sup>4,38</sup>. To further quantify genetic correlation between organoids and corresponding tumors, we analyzed somatic single nucleotide variants (SNVs) and structural variants (SVs). Most SNVs and SVs present in the original tumor were maintained in the organoids derived thereof, and vice versa (Extended Data Figs. 4b and 5a). Shared mutations were also maintained after extended passaging (Extended Data Fig. 4b). Some organoid lines, such as HGS-19, HGS-3.1 and MC-2.1, presented marked differences with their corresponding tumor sample (Extended Data Fig. 5a). We believe that these differences result from low tumor cell content within the original tumor samples as evident from their low number of SNVs, SVs and the lack of obvious CNVs (Extended Data Fig. 4).

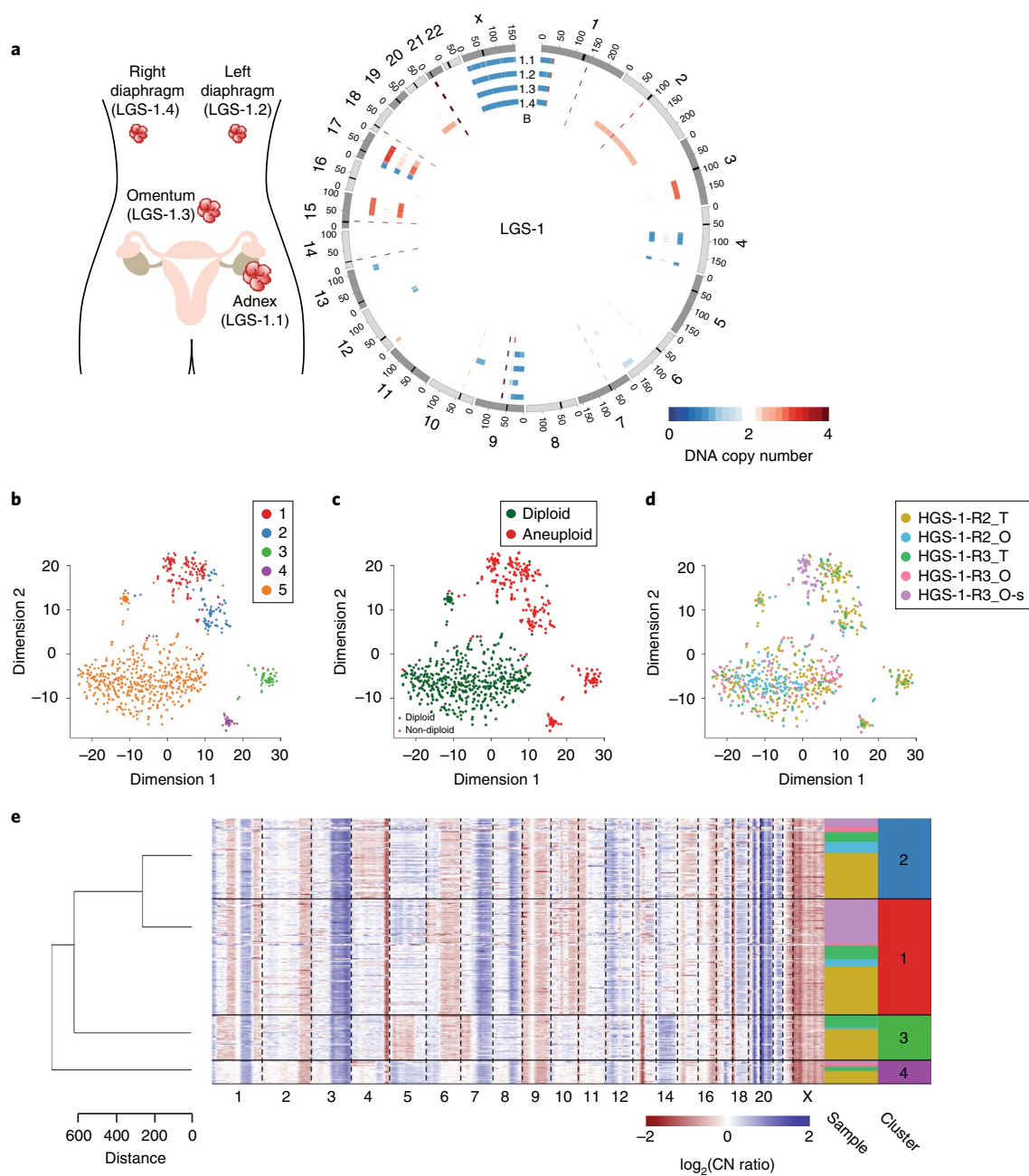


**Fig. 4 | OC organoids capture tumor heterogeneity.** **a**, Schematic of tumor locations and a circos plot presenting CNV events (red, gain; blue, loss) in the organoid lines derived from a patient diagnosed with LGS OC. Outside to inside: genomic position, LGS-1.1 (adnex tumor), LGS-1.2 (metastasis left diaphragm), LGS-1.3 (metastasis omentum), LGS-1.4 (metastasis right diaphragm), blood germline reference. **b**, *t*-SNE plot of single-cell CNV profiles from two recurrent tumor samples and corresponding organoid lines (HGS-1-R2, HGS-1-R3) of a single patient. Hierarchical clustering has separated the cells into five different clusters (color coded). Total number of analyzed cells is 791. **c**, *t*-SNE plot presenting diploid (green) and aneuploid (red) cells. Total number of analyzed cells is 791. **d**, Single-cell distribution into the different clusters according to sample of origin. T, tumor; O, organoid; -s, second time point analysis. HGS-1-R2\_T,  $n=351$  cells; HGS-1-R2\_O, passage 5,  $n=159$  cells; HGS-1-R3\_T,  $n=93$  cells; HGS-1-R3\_O, passage 4,  $n=122$  cells; HGS-1-R3\_O, passage 12,  $n=66$  cells. **e**, Clustered CNV heat map of aneuploid cells presenting gains (blue) and losses (red) across the genome. Sample origin and cluster belonging of each cell is color coded.

Next, we tested whether organoids displayed known OC-associated somatic mutations, amplifications and deletions. Somatic mutations in *KRAS* and *BRAF* genes, which are frequently found in MC and LGS tumors<sup>39,40</sup>, were identified in the corresponding organoid subtypes (MC-1, MC-2 (*KRAS*), LGS-5 (*BRAF*); Fig. 3 and Supplementary Table 7). Moreover, all organoids derived from HGS tumors showed non-silent mutations including missense, stop gain and frameshifts in the *TP53* gene, in some cases accompanied by the loss of the second

allele (Fig. 3 and Supplementary Table 7). Amplifications of *MYC* and *CCNE1* as well as loss of *RBI*, *PTEN* and *CDKN2A/B* genes (frequent in HGS tumors<sup>5,41</sup>) were observed (Fig. 3). These oncogenic modifications were mostly conserved between organoids and corresponding tumors (Fig. 3 and Supplementary Table 7).

DNA methylation analysis was performed on a subset of organoids at early and late time points, using Illumina Infinium methylationEPIC 850K BeadChip. Clustering of these organoid

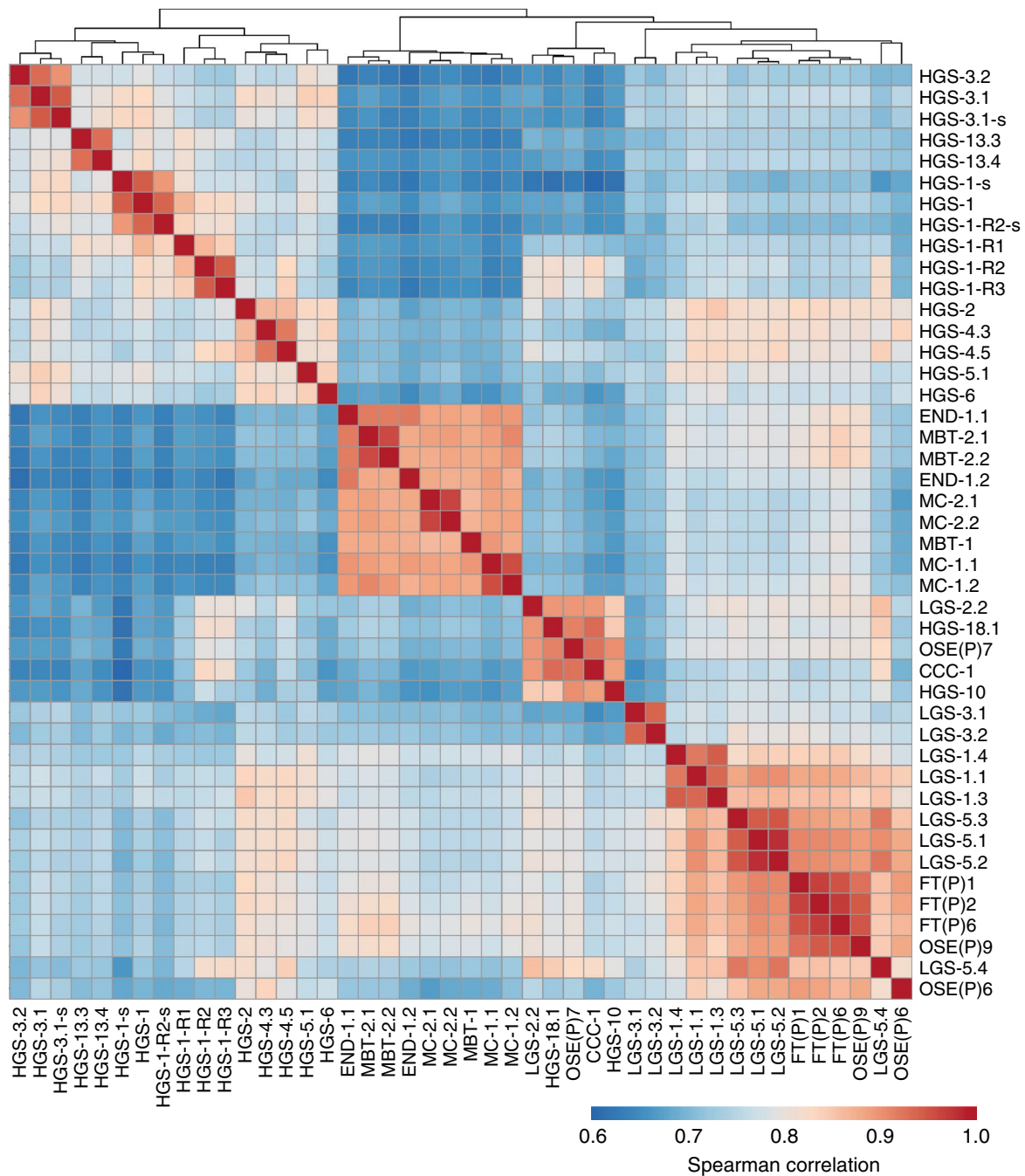


**Fig. 5 | Gene expression analysis of OC organoids.** Heat map of Spearman correlation values of normal FT ( $n = 3$  independent FT lines), OSE ( $n = 3$  independent OSE lines), non-malignant BTs ( $n = 3$  independent MBT lines) and malignant organoid lines ( $n = 32$  independent malignant lines), based on RNA-seq expression data. Read counts were normalized for sequencing depth and the 5,000 most-variable genes were used. For three organoid lines, a second time point was analyzed after extended passaging, demonstrating high correlation with early passaged organoids. -, second time point analysis. HGS-1: passage 8 and 32; HGS-3.2: passage 4 and 32; HGS-1-R2: passage 4 and 17. Passage number in which all organoid lines were sequenced is given in Supplementary Table 7.

samples based on the methylation beta-values demonstrated that organoids maintained their epigenetic profile after extended passaging (Extended Data Fig. 5b), as found previously for colorectal cancer organoids<sup>23</sup>.

**OC organoids capture tumor heterogeneity.** To assess whether organoids capture inpatient heterogeneity, we compared organoid lines derived from one primary and three metastatic sites of a patient diagnosed with LGS OC (Fig. 4a). CNV analysis revealed

losses and gains shared by all tumor lesions from the same patient (for example, loss of chromosome X) as well as copy number changes only present in the metastatic sites (for example, loss of 17p in LGS-1.2,3,4; Fig. 4a). These CNVs are conserved between tumor tissue and the corresponding organoids (Extended Data Fig. 4a) and, therefore, appear to represent genomic changes that occurred at different time points along the course of tumor evolution.

We next tested whether tumor heterogeneity is maintained within an organoid line using a novel single-cell DNA sequencing

method (see Methods) and sequenced 791 cells from 2 recurrent tumor samples (HGS-1-R2 and HGS-1-R3; both were derived from a single patient at different time points) and corresponding organoid lines from either one or two time points (HGS-1-R2, passage 5; HGS-1-R3, passage 4 and 12). Calculation of CNV profiles for each cell was followed by independent component analysis that revealed five distinct clusters (Fig. 4b). Clusters 1–4 comprised aneuploid cells whereas cluster 5 comprised diploid cells (Fig. 4c). As expected, tumor samples that were obtained from ascites drainage of a single patient within a 1 month interval overlapped with each other and did not form separate clusters (Fig. 4d), thus validating the robustness of the single-cell DNA sequencing method. Organoid-derived cells overlapped with the same 5 clusters (albeit with low representation in cluster 3) demonstrating both their heterogeneity and resemblance to the original tumor samples (Fig. 4d). HGS-1-R3 relative cell abundance in cluster 5 (diploid cells) was dramatically reduced after extended passaging (passage 4 versus 12), whereas representation of clusters 1, 2 and 4 (aneuploid cells) increased (Fig. 4d,e), suggesting that tumor cells overgrew normal cells over time, while maintaining tumor heterogeneity.

**Gene expression analysis of OC organoids.** To assess organoid gene expression profiles, we performed RNA sequencing (RNA-seq) on 35 OC organoids, and 6 normal OSE and FT organoids. Hierarchical clustering assigned organoids to three independent main groups, representing (1) HGS carcinomas, (2) MC and END tumors and (3) mainly LGS carcinomas, FT and OSE (Fig. 5). Organoids derived from multiple tumor lesions of the same patient were transcriptionally more similar to each other than to unrelated organoid lines (for example, MC-1.1,2 and HGS-3.1,2). In a similar manner, organoids that were sequenced at a second time point after extended passaging clustered with their corresponding samples (HGS-1, passage 8 versus 32; HGS-3.1, passage 4 versus 32; HGS-1-R2 passage 4 versus 17). Of note, non-malignant MBT and malignant MC organoids clustered together. This was seen in eight organoid lines derived from four different patients (two MC and two MBT), suggesting a biological link between these samples. This finding is in agreement with a causality hypothesis that suggests a stepwise progression from BTs to invasive carcinomas<sup>42–44</sup>. Furthermore, OSE(P)7 organoids (derived from a sample collected during risk-reducing salpingo-oophorectomy) clustered together with OC organoids and apart from normal OSE and FT organoid

lines. This finding, together with morphological, histological and metaphase spread analysis (Extended Data Fig. 3e,f), suggested that OSE(P)7 consists of malignant cells that were not diagnosed by routine pathological examination.

**Genetic manipulation and drug screening of OC organoids.** To demonstrate the experimental potential of OC organoids, we next adapted genetic manipulation techniques and drug-screening methods for normal FT and OC organoids.

Normal FT organoids were electroporated with pSpCas9(BB)-2A-GFP plasmid into which we cloned a guide RNA targeting the *TP53* gene (Extended Data Fig. 6a). Thus, we could determine the electroporation efficiency by monitoring GFP expression (Extended Data Fig. 6c,d) and target the *TP53* gene, which is believed to be mutated at an early time point in the course of HGS tumor development. Three days after electroporation, nutlin3a (which inhibits MDM2–p53 interaction<sup>45</sup> and, therefore, kills *TP53* wild-type clones) was added to the medium (Extended Data Fig. 6a,b). Surviving clones were picked, clonally expanded and analyzed for *TP53* mutations (Extended Data Fig. 6e). As a result, multiple clones harboring mutations in *TP53* from carriers of *BRCA* germline mutations were established (Extended Data Fig. 6f). In a similar manner, we have electroporated FT organoids with plasmids targeting both *TP53* and *RB1* genes and established clones in which both genes were knocked out (Extended Data Fig. 6f). Clone expansion was accompanied by morphological alterations including transition from cystic to denser organoids and increased cell shedding into the organoid lumen (Extended Data Fig. 6g). Hierarchical clustering based on RNA-seq assigned the clones into different clusters according to their genetic modifications (Extended Data Fig. 6h).

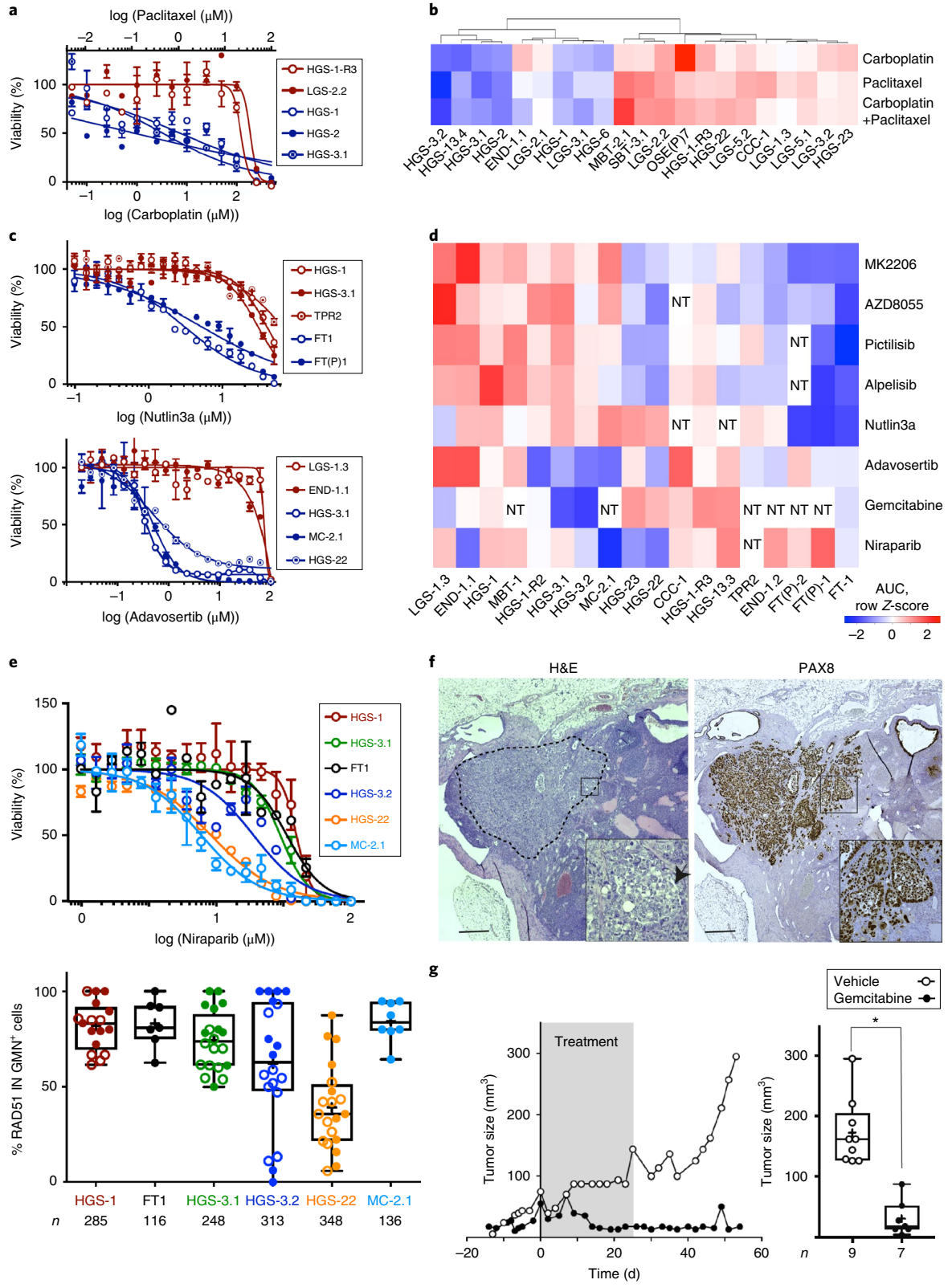
To demonstrate that OC organoids can be genetically modified in a stable manner, they were transduced with a lentiviral vector driving expression of fluorescently tagged histone-2B (H2B-Neon). H2B-Neon-transduced organoids enabled three-dimensional live cell imaging of mitosis and revealed multiple aberrant chromosomal segregation events (Supplementary Videos 2–6).

Next, we tested organoid sensitivity to platinum/taxane drugs that are commonly used in OC treatment protocols, that is carboplatin, paclitaxel, as well as non-platinum/taxane drugs that previously have been suggested as possible treatments for OC. The drug panel included drugs targeting the PI3K/AKT/mTOR

**Fig. 6 | In vitro and in vivo drug sensitivity assays.** **a**, Representative dose–response curves of HGS and LGS organoid lines treated with carboplatin/paclitaxel. Organoid line derived from a recurrent disease (HGS-1-R3) show acquired resistance. Dots represent the mean of technical duplicates. Error bars represent s.e.m. of technical duplicates. **b**, Heat map of Euclidean distance of 21 distinct organoid lines, based on AUC row Z-score values. As expected, most HGS OC organoids (6 out of 9) are more sensitive to carboplatin/paclitaxel drugs compared with non-HGS OC organoids (9 out of 12). The HGS-1 organoid line is sensitive to carboplatin/paclitaxel drugs, whereas the matching recurrent organoid line (HGS-1-R3) is resistant. **c**, Representative dose–response curves for nutlin3a (top) and adavosertib (bottom). Normal FT organoids show high sensitivity for nutlin3a, whereas HGS and genetically modified FT line, which are mutated in the *TP53* gene, are resistant. Dots represent the mean of technical duplicates. Error bars represent s.e.m. of technical duplicates. **d**, Heat map of Euclidean distance, based on AUC row Z-score values, showing organoid response to a panel of drugs, including PI3K/AKT/mTOR pathway, PARP and Wee1 inhibitors.  $n=18$  distinct organoid lines. NT, not tested. **e**, Top, dose–response curves for niraparib show differential response between organoid lines. Dots represent the mean of technical duplicates. Error bars represent s.e.m. of technical duplicates. Bottom, box-and-whisker plot (minimum to maximum) presenting RAD51 foci score after radiation. Each point represents percentage of RAD51+ cells within geminin+ (GMN+) cell population in one organoid. Horizontal bars and ‘+’ represent median and mean of all dots, respectively. Empty and full dots show results of two biologically independent experiments conducted one or two passages apart. Total number ( $n$ ) of analyzed geminin+ cells in each organoid line is presented. **f**, Histological analysis of organoid-derived xenograft (HGS-3.1) following orthotopic transplantation into the mouse bursa. Tumor cells have invaded into the mouse ovary and H&E staining (left) shows solid pattern with indications for slit-like spaces (arrow) as well as pleomorphic cells with prominent nuclear atypia. Xenograft has maintained PAX8-positive staining (right). A summary of organoid-derived xenograft experiments is presented in Supplementary Table 8. Scale bar, 0.5 mm. **g**, Gemcitabine-sensitive organoids were subcutaneously injected into immunodeficient mice and tumor size was monitored. Once the tumor reached 50 mm<sup>3</sup>, mice were randomly selected and treated with intraperitoneal injections of gemcitabine (2 mg per kg body weight) ( $n=7$  independent mice) or vehicle ( $n=9$  independent mice), 5 times per week for 4 consecutive weeks (in total 20 injections). Left, an example of tumor growth over time in a vehicle (white dots) and a gemcitabine-treated (black dots) mouse. Right, box-and-whisker plot (minimum to maximum) summarizing the results across all vehicle and gemcitabine-treated mice, showing tumor size at day 55. Horizontal bars and ‘+’ represent median and mean of all dots, respectively. \* $P<0.001$ ,  $t$ -test.

pathway (alpelisib, pictilisib, MK2206, AZD8055), poly (ADP-ribose) polymerase (PARP) (Niraparib), the tyrosine kinase Wee1 (adavosertib) and gemcitabine. Organoids were disrupted into small clumps and dispensed into 384-well plates pre-coated with BME. A cell viability assay was performed 5 d after the drugs were added and organoid drug sensitivity was represented by

the average area under the dose-response curve (AUC) of two technical replicates<sup>46</sup>. Assay quality was confirmed by calculating plate Z-factor across all plates (mean = 0.61; Extended Data Fig. 5e) and by the correlation of AUC between technical and biological replicates (Pearson correlation = 0.94, 0.87, respectively; Extended Data Fig. 5c,d).



Unsupervised hierarchical clustering based on platinum/taxane drug sensitivity divided the organoids into two main clusters: sensitive lines that consisted primarily of HGS organoids and resistant lines that consisted primarily of non-HGS organoids (Fig. 6b). Notably, the HGS-1-R3 line, which was derived from ascites of recurrent disease, clinically resistant to chemotherapy (Supplementary Table 1), clustered together with the resistant cluster. HGS-1 line, which was derived from the primary, chemotherapy-sensitive tumor of the same patient clustered with the sensitive cluster (Fig. 6a,b).

Since the *TP53* gene is mutated in the vast majority of OC, we tested whether nutlin3a can serve to rapidly distinguish between wild-type and mutated *TP53* OC organoids. In total, 16 organoid lines were tested (3 normal FT lines, 1 genetically modified FT clone and 13 OC lines). As expected, all FT organoid lines were highly sensitive to nutlin3a treatment whereas the genetically modified clone in which we knocked out the *TP53* gene and the OC lines (with one exception) were resistant (Fig. 6c,d). The only OC line that was sensitive to nutlin3a, was LGS-1.3 and in this organoid, indeed no point mutation in the *TP53* gene was identified (Supplementary Table 7).

Drug-screening assays demonstrated differential drug responses of individual organoid lines (Fig. 6a–e). For example, HGS-3.1 organoid line was highly sensitive to gemcitabine, adavosertib, carboplatin and paclitaxel and resistant to drugs that target the PI3K/AKT/mTOR pathway, whereas HGS-23 line demonstrated the opposite drug sensitivity pattern (Fig. 6a–d).

Homologous recombination-deficient cells have been shown to be sensitive to PARP inhibitors<sup>47,48</sup>. To determine whether this correlation is also present in OC organoids, a subset of organoid lines with differential responses to niraparib (Fig. 6e) was tested for homologous recombination by using the recombination capacity (RECAP) test, which assesses homologous recombination capacity using accumulation of RAD51 protein at sites of DNA double-strand breaks<sup>49</sup>. Organoids were irradiated with 5 Gy X-rays, recovered for 2 h, fixed and stained with antibodies against RAD51 and geminin (a marker for S/G2 phases of the cell cycle). The percentage of geminin<sup>+</sup> cells with RAD51 foci was scored blinded for sensitivity to niraparib. Organoids with a low percentage of geminin<sup>+</sup> cells with RAD51 foci were more sensitive to niraparib compared with organoids with a high percentage of geminin<sup>+</sup> cells with RAD51 foci (with the exception of MC-2.1) (Fig. 6e).

**Xenotransplantation of OC organoids and in vivo drug sensitivity.** We next tested whether OC organoid can be orthotopically or subcutaneously transplanted into immunodeficient mice. For orthotopic transplantations, organoids were transduced with a lentiviral vector encoding luciferase and transplanted into the mouse bursa. Bioluminescence imaging was used to validate tumor growth (Extended Data Fig. 5f). All three lines that were orthotopically transplanted grew into a tumor (Supplementary Table 8). Six out of seven lines were successfully transplanted subcutaneously (Supplementary Table 8). Histological analysis of orthotopically transplanted HGS carcinoma organoid line demonstrated that the tumor invaded the ovary, displayed prominent nuclear atypia, slit-like spaces and maintained PAX8 and p53 staining (Fig. 6f and Extended Data 5g). The MC organoid line that was subcutaneously transplanted showed characteristics of a MC tumor including goblet cells and haphazardly arranged neoplastic glands lined by columnar cells (Extended Data Fig. 5h).

To validate whether in vitro drug sensitivity is recapitulated in vivo, we chose the HGS-3.1 organoid line that was highly sensitive to gemcitabine (Fig. 6c), a nucleoside analog that is in clinical use for HGS OC. Organoids were subcutaneously injected and tumor size was monitored. Once it reached 50 mm<sup>3</sup>, mice were randomly selected and treated with vehicle or gemcitabine. While tumors continued growing in vehicle-treated mice, tumor growth was com-

pletely blocked or reduced in gemcitabine-treated mice, as indicated by tumor size measured at the end of the experiment (vehicle and gemcitabine-treated mice,  $n=9$  and  $n=7$ , respectively) (Fig. 6g).

## Discussion

Developing reliable experimental models that address clinical challenges, such as early detection, tumor recurrence and acquired chemotherapy resistance, is a high priority in OC research<sup>2</sup>. In this study, we describe an organoid platform that enables long-term in vitro expansion, manipulation and analysis of a wide variety of OC subtypes. A comprehensive analysis demonstrates that OC organoids maintain tumor histological characteristics, such as nuclear and cellular atypia, and biomarker expression, such as p53 and PAX8. Organoids and corresponding tumors remained highly similar at the genomic level, even after extended passaging. Furthermore, organoids recapitulated OC hallmarks, such as CNVs, recurrent mutations and tumor heterogeneity. Finally, unsupervised hierarchical clustering of gene expression data grouped the organoids according to their tumor type and demonstrated that LGS organoids are more similar to normal samples than are HGS lines.

During organoid biobanking of normal FT and OSE samples, obtained from risk-reducing surgeries, we encountered two samples that were apparently malignant: LGS-2 (clinically diagnosed) and OSE(P)7 (indicated by organoid characterization, Extended Data Fig. 3e,f). Interestingly, unsupervised hierarchical clustering of gene expression data grouped these organoid lines together, thus implying biological similarity. Both organoid lines were derived from patients at high risk of developing HGS tumors. Therefore, these samples potentially represent an early time point in HGS development. Establishing and analyzing additional early/pre-malignant organoid lines from pBSO material might substantiate this hypothesis and provide a unique opportunity to study early HGS tumor development.

An additional experimental platform, recently described to model colorectal cancer development<sup>50–53</sup>, can be established through CRISPR-mediated mutation of tumor driver genes in normal organoids. Indeed, we demonstrate that normal FT organoids from OC high-risk donors can be efficiently CRISPR–Cas9 genome edited and clonally expanded afterwards, demonstrating the feasibility of such an approach in OC.

HGS tumors are frequently sensitive to platinum-based chemotherapy, whereas non-HGS tumors (such as LGS and MC tumors) are characterized by relative chemoresistance<sup>54–57</sup>. Consistent with these clinical observations, most HGS organoids were sensitive to platinum-based treatments, whereas non-HGS organoids (that is MBT, SBT and LGS) were more resistant (Fig. 6b). In one case, we compared drug responses in matched organoid lines derived from primary chemosensitive (HGS-1) and recurrent chemoresistant (HGS-1-R3) tumors of a single patient. This experiment confirmed an increased resistance of the organoid line derived from the recurrent tumor to platinum-based chemotherapy, anecdotally substantiating the clinical relevance of OC organoids. Increasing the number of matched primary/recurrent organoid pairs is currently ongoing. The individual drug responses of OC organoids (for example, compare HGS-23- and HGS-3.1) illustrates the complexity of choosing the right treatment. We provide proof of concept that in vitro drug sensitivity of OC organoid can be tested following xenotransplantation.

In summary, we present a new organoid culture-based platform for the study of OC that supports efficient derivation and long-term in vitro expansion of a wide variety of OC subtypes. This living OC organoid biobank—available to the research community—faithfully recapitulates OC hallmarks, can be subjected to genetic manipulations and to drug screening and opens the door to many avenues of OC research.

### Online content

Any methods, additional references, Nature Research reporting summaries, source data, extended data, supplementary information, acknowledgements, peer review information; details of author contributions and competing interests; and statements of data and code availability are available at <https://doi.org/10.1038/s41591-019-0422-6>.

Received: 28 November 2017; Accepted: 12 March 2019;

Published online: 22 April 2019

### References

- Vaughan, S. et al. Rethinking ovarian cancer: recommendations for improving outcomes. *Nat. Rev. Cancer* **11**, 719–725 (2011).
- Bowtell, D. D. et al. Rethinking ovarian cancer II: reducing mortality from high-grade serous ovarian cancer. *Nat. Rev. Cancer* **15**, 668–679 (2015).
- Fischerova, D. et al. Diagnosis, treatment, and follow-up of borderline ovarian tumors. *Oncologist* **17**, 1515–1533 (2012).
- Koshiyama, M., Matsumura, N. & Konishi, I. Recent concepts of ovarian carcinogenesis: type I and type II. *Biomed. Res. Int.* **2014**, 934261 (2014).
- Cancer Genome Atlas Research Network Integrated genomic analyses of ovarian carcinoma. *Nature* **474**, 609–615 (2011).
- Ciriello, G. et al. Emerging landscape of oncogenic signatures across human cancers. *Nat. Genet.* **45**, 1127–1133 (2013).
- Piek, J. M. et al. Dysplastic changes in prophylactically removed Fallopian tubes of women predisposed to developing ovarian cancer. *J. Pathol.* **195**, 451–456 (2001).
- Kurman, R. J. & Shih Ie, M. The origin and pathogenesis of epithelial ovarian cancer: a proposed unifying theory. *Am. J. Surg. Pathol.* **34**, 433–443 (2010).
- Thu, K. L. et al. A comprehensively characterized cell line panel highly representative of clinical ovarian high-grade serous carcinomas. *Oncotarget* **8**, 50489–50499 (2017).
- Fleury, H. et al. Novel high-grade serous epithelial ovarian cancer cell lines that reflect the molecular diversity of both the sporadic and hereditary disease. *Genes Cancer* **6**, 378–398 (2015).
- Ince, T. A. et al. Characterization of twenty-five ovarian tumour cell lines that phenocopy primary tumours. *Nat. Commun.* **6**, 7419 (2015).
- Letourneau, I. J. et al. Derivation and characterization of matched cell lines from primary and recurrent serous ovarian cancer. *BMC Cancer* **12**, 379 (2012).
- Kreuzinger, C. et al. Molecular characterization of 7 new established cell lines from high grade serous ovarian cancer. *Cancer Lett.* **362**, 218–228 (2015).
- Sachs, N. & Clevers, H. Organoid cultures for the analysis of cancer phenotypes. *Curr. Opin. Genet. Dev.* **24**, 68–73 (2014).
- Domcke, S. et al. Evaluating cell lines as tumour models by comparison of genomic profiles. *Nat. Commun.* **4**, 2126 (2013).
- Jones, P. M. & Drapkin, R. Modeling high-grade serous carcinoma: how converging insights into pathogenesis and genetics are driving better experimental platforms. *Front. Oncol.* **3**, 217 (2013).
- Ben-David, U. et al. Patient-derived xenografts undergo mouse-specific tumor evolution. *Nat. Genet.* **49**, 1567–1575 (2017).
- Sato, T. et al. Long-term expansion of epithelial organoids from human colon, adenoma, adenocarcinoma, and Barrett's epithelium. *Gastroenterology* **141**, 1762–1772 (2011).
- Gao, D. et al. Organoid cultures derived from patients with advanced prostate cancer. *Cell* **159**, 176–187 (2014).
- Fujii, M. et al. A colorectal tumor organoid library demonstrates progressive loss of niche factor requirements during tumorigenesis. *Cell Stem Cell* **18**, 827–838 (2016).
- Boj, S. F. et al. Organoid models of human and mouse ductal pancreatic cancer. *Cell* **160**, 324–338 (2015).
- van de Wetering, M. et al. Prospective derivation of a living organoid biobank of colorectal cancer patients. *Cell* **161**, 933–945 (2015).
- Roerink, S. F. et al. Intra-tumour diversification in colorectal cancer at the single-cell level. *Nature* **556**, 457–462 (2018).
- Vlachogiannis, G. et al. Patient-derived organoids model treatment response of metastatic gastrointestinal cancers. *Science* **359**, 920–926 (2018).
- Sachs, N. et al. A living biobank of breast cancer organoids captures disease heterogeneity. *Cell* **172**, 373–386.e10 (2018).
- Verissimo, C. S. et al. Targeting mutant RAS in patient-derived colorectal cancer organoids by combinatorial drug screening. *Elife* **5**, e18489 (2016).
- Hill, S. J. et al. Prediction of DNA repair inhibitor response in short term patient-derived ovarian cancer organoids. *Cancer Discov.* **8**, 1404–1421 (2018).
- Kessler, M. et al. The Notch and Wnt pathways regulate stemness and differentiation in human fallopian tube organoids. *Nat. Commun.* **6**, 8989 (2015).
- Gilmour, L. M. et al. Neuregulin expression, function, and signaling in human ovarian cancer cells. *Clin. Cancer Res.* **8**, 3933–3942 (2002).
- Aune, G. et al. Increased circulating hepatocyte growth factor (HGF): a marker of epithelial ovarian cancer and an indicator of poor prognosis. *Gynecol. Oncol.* **121**, 402–406 (2011).
- Sheng, Q. et al. An activated ErbB3/NRG1 autocrine loop supports in vivo proliferation in ovarian cancer cells. *Cancer Cell* **17**, 298–310 (2010).
- Bourgeois, D. L. et al. High-grade serous ovarian cancer cell lines exhibit heterogeneous responses to growth factor stimulation. *Cancer Cell Int.* **15**, 112 (2015).
- Antoniou, A. et al. Average risks of breast and ovarian cancer associated with *BRCA1* or *BRCA2* mutations detected in case series unselected for family history: a combined analysis of 22 studies. *Am. J. Hum. Genet.* **72**, 1117–1130 (2003).
- Gabai-Kapara, E. et al. Population-based screening for breast and ovarian cancer risk due to *BRCA1* and *BRCA2*. *Proc. Natl Acad. Sci. USA* **111**, 14205–14210 (2014).
- Wang, M. et al. PAX2 and PAX8 reliably distinguishes ovarian serous tumors from mucinous tumors. *Appl. Immunohistochem. Mol. Morphol.* **23**, 280–287 (2015).
- Rajagopalan, H. & Lengauer, C. Aneuploidy and cancer. *Nature* **432**, 338–341 (2004).
- Priestley, P. et al. Pan-cancer whole genome analyses of metastatic solid tumors. Preprint at <https://doi.org/10.1101/415133> (2018).
- Gorringe, K. L. et al. High-resolution single nucleotide polymorphism array analysis of epithelial ovarian cancer reveals numerous microdeletions and amplifications. *Clin. Cancer Res.* **13**, 4731–4739 (2007).
- Hunter, S. M. et al. Pre-invasive ovarian mucinous tumors are characterized by CDKN2A and RAS pathway aberrations. *Clin. Cancer Res.* **18**, 5267–5277 (2012).
- Romero, I. et al. Low-grade serous carcinoma: new concepts and emerging therapies. *Gynecol. Oncol.* **130**, 660–666 (2013).
- Kuo, K. T. et al. Analysis of DNA copy number alterations in ovarian serous tumors identifies new molecular genetic changes in low-grade and high-grade carcinomas. *Cancer Res.* **69**, 4036–4042 (2009).
- Seidman, J. D. et al. The fallopian tube–peritoneal junction: a potential site of carcinogenesis. *Int. J. Gynecol. Pathol.* **30**, 4–11 (2011).
- Kurman, R. J. & Shih Ie, M. Molecular pathogenesis and extraovarian origin of epithelial ovarian cancer—shifting the paradigm. *Hum. Pathol.* **42**, 918–931 (2011).
- Seidman, J. D. & Khedmati, F. Exploring the histogenesis of ovarian mucinous and transitional cell (Brenner) neoplasms and their relationship with Walthard cell nests: a study of 120 tumors. *Arch. Pathol. Lab. Med.* **132**, 1753–1760 (2008).
- Vassilev, L. T. et al. In vivo activation of the p53 pathway by small-molecule antagonists of MDM2. *Science* **303**, 844–848 (2004).
- Yadav, B. et al. Quantitative scoring of differential drug sensitivity for individually optimized anticancer therapies. *Sci. Rep.* **4**, 5193 (2014).
- Lord, C. J. & Ashworth, A. PARP inhibitors: synthetic lethality in the clinic. *Science* **355**, 1152–1158 (2017).
- Murai, J. Targeting DNA repair and replication stress in the treatment of ovarian cancer. *Int. J. Clin. Oncol.* **22**, 619–628 (2017).
- Meijer, T. G. et al. Functional ex vivo assay reveals homologous recombination deficiency in breast cancer beyond *BRCA* gene defects. *Clin. Cancer Res.* **24**, 6277–6287 (2018).
- Drost, J. et al. Sequential cancer mutations in cultured human intestinal stem cells. *Nature* **521**, 43–47 (2015).
- Matano, M. et al. Modeling colorectal cancer using CRISPR-Cas9-mediated engineering of human intestinal organoids. *Nat. Med.* **21**, 256–262 (2015).
- Drost, J. et al. Use of CRISPR-modified human stem cell organoids to study the origin of mutational signatures in cancer. *Science* **358**, 234–238 (2017).
- Fumagalli, A. et al. Genetic dissection of colorectal cancer progression by orthotopic transplantation of engineered cancer organoids. *Proc. Natl Acad. Sci. USA* **114**, E2357–E2364 (2017).
- Schmeler, K. M. et al. Neoadjuvant chemotherapy for low-grade serous carcinoma of the ovary or peritoneum. *Gynecol. Oncol.* **108**, 510–514 (2008).
- Gershenson, D. M. et al. Recurrent low-grade serous ovarian carcinoma is relatively chemoresistant. *Gynecol. Oncol.* **114**, 48–52 (2009).
- Pectasides, D. et al. Advanced stage mucinous epithelial ovarian cancer: the Hellenic Cooperative Oncology Group experience. *Gynecol. Oncol.* **97**, 436–441 (2005).
- Brown, J. & Frumovitz, M. Mucinous tumors of the ovary: current thoughts on diagnosis and management. *Curr. Oncol. Rep.* **16**, 389 (2014).

### Acknowledgements

We thank T. Bayram for supporting of ethical regulatory affairs. We acknowledge A. Brousalı, P. van der Groep, A. Constantinides, A. Snelting and O. Kranenburg of the Utrecht Platform for Organoid Technology (U-PORT; UMC Utrecht) for patient inclusion and tissue acquisition. We thank the Integraal Kankercentrum Nederland

(IKNL) and M. van der Aa for supplying clinical data, and I. Renkens for help with DNA isolations. We acknowledge E. Stelloo for her help with culturing organoids. We thank the people from the Preclinical Intervention Unit of the Mouse Clinic for Cancer and Ageing (MCCA) at the NKI for performing the intervention studies. We thank B. Artegiani and T. Dayton for critically reading the manuscript. O.K. was supported by Marie Skłodowska-Curie IF grant 658933 – HGSOC. This work was funded by the gravitation program CancerGenomiCs.nl from the Netherlands Organisation for Scientific Research (NWO), MKMD grant (114021012) from Netherlands Organization for Scientific Research (NWO-ZonMw), Stand Up to Cancer International Translational Cancer Research Grant, a program of the Entertainment Industry Foundation administered by the AACR, Dutch Cancer Society (KWF) grant UU2015-7743, Dutch Cancer Society (Alpe d'HuZes) grant EMCR 2014-7048, and a grant from the Gieskes Strijbis Foundation (1816199). The Onco Institute is supported by the Dutch Cancer Society.

### Author contributions

Conceptualization: O.K. and H.C. Methodology: O.K. and H.C. Software: J.E.V.-I., M.J.v.R., L.K. and W.P.K. Formal analysis: O.K., K.L., N.H., J.E.V.-I., M.J.v.R., T.J., P.J.V.D., S.A.R., L.K. and W.P.K. Investigation: O.K., K.L., C.J.d.W., N.H., A.V.B., H.B., J.K., S.A.R., L.K., N.P., R.T., L.M.v.W. and B.P. Resources: C.J.d.W., L.M.v.W., H.V., M.P.G.V., V.W.H.H., B.G.N., P.O.W., M.V.D.V., T.B., K.N.G. and R.P.Z. Data curation: O.K.,

C.J.d.W. and J.E.V.-I. Writing—original draft: O.K., C.J.d.W., J.E.V.-I., W.P.K. and H.C. Visualization: O.K., C.J.d.W., K.L., J.E.V.-I., W.P.K., L.K. and N.H. Supervision: M.V.D.V., J.L.B., R.P.Z., H.J.G.S., W.P.K., A.v.O. and H.C. Project administration: O.K., C.J.d.W., W.P.K. and H.C. Funding acquisition: J.L.B., R.P.Z., P.O.W., W.P.K. and H.C.

### Competing interests

The authors declare no competing interests.

### Additional information

**Extended data** is available for this paper at <https://doi.org/10.1038/s41591-019-0422-6>.

**Supplementary information** is available for this paper at <https://doi.org/10.1038/s41591-019-0422-6>.

**Reprints and permissions information** is available at [www.nature.com/reprints](http://www.nature.com/reprints).

**Correspondence and requests for materials** should be addressed to W.P.K. or H.C.

**Publisher's note:** Springer Nature remains neutral with regard to jurisdictional claims in published maps and institutional affiliations.

© The Author(s), under exclusive licence to Springer Nature America, Inc. 2019

## Methods

**Approval of studies involving humans and patient-informed consent.** The collection of patient data and tissue for the generation and distribution of normal FT, OSE and OC organoids was performed according to the guidelines of the European Network of Research Ethics Committees (EUREC) following European, national and local law. The medical ethical committee UMC Utrecht (METC UMCU) approved the biobanking protocol: 14-472 HUB-OVI. All patients participating in this study signed informed consent forms and could withdraw their consent at any time.

Available organoids are cataloged at [www.hub4organoids.eu](http://www.hub4organoids.eu) and can be requested at [info@hub4organoids.eu](mailto:info@hub4organoids.eu). Distribution of organoids to third parties will have to be authorized by the METC UMCU at request of the HUB to ensure compliance with the Dutch 'medical research involving human subjects' act.

**OC tissue processing.** On arrival, OC tissues were cut into 3–5 mm<sup>3</sup> pieces (Extended Data Fig. 1a). Two or three random pieces were snap frozen and stored at –80 °C for DNA isolation, two random pieces were fixed in formalin for histopathological analysis and immunohistochemistry, and the remainder were processed for organoid derivation. For organoid derivation: tissue was minced, washed with 10 ml AdDF+++ (Advanced DMEM/F12 containing 1x Glutamax, 10 mM HEPES and antibiotics). We let big tissue pieces to sink to tube bottom with gravity (for 2–5 min), collected the supernatant and centrifuged at 1,000 r.p.m. for 5 min. In case of a visible red pellet, erythrocytes were lysed in 2 ml red blood cell lysis buffer (Roche, 11814389001) for 5 min at room temperature followed by an additional wash with 10 ml AdDF+++ and centrifugation at 1,000 r.p.m. Remaining big tissue pieces were digested in 5–10 ml AdDF+++ supplemented with 5 μM RHO/ROCK pathway inhibitor (Abmole Bioscience, Y-27632) containing 0.5–1.0 mg ml<sup>–1</sup> collagenase (Sigma, C9407) on an orbital shaker at 37 °C for 0.5–1.0 h. The digested tissue suspension was sheared using 5 ml plastic pipettes. Suspension was strained over a 100 μm filter and large tissue pieces entered a subsequent digestion and shearing step. Suspension was centrifuged at 1,000 r.p.m. and the pellet was resuspended in 10 ml AdDF+++ and centrifuged again at 1,000 r.p.m. Once again, in case of a visible red pellet, erythrocytes were lysed in 2 ml red blood cell lysis buffer for 5 min at room temperature followed by an additional wash with 10 ml AdDF+++ and centrifugation at 1,000 r.p.m.

Ascites/pleural effusion samples were centrifuged at 1,000 r.p.m. and treated with 2 ml red blood cell lysis buffer for 5 min at room temperature. Following erythrocyte lysis, 10 ml AdDF+++ was added and suspension was centrifuged at 1,000 r.p.m.

Following removal of large part of the ovarian stroma and the surrounding muscle layers of FT, ovary and FT samples were processed as above.

**Organoid culture.** The cell pellet was suspended in 10 mg ml<sup>–1</sup> cold Cultrex growth factor reduced BME type 2 (Trevigen, 3533-010-02) and 40 μl drops of BME cell suspension were allowed to solidify on pre-warmed 24-well suspension culture plates (Greiner, M9312) at 37 °C for 30 min. On BME stabilization, 500 ml of appropriate organoid medium (OC/OCwnt/OSE/FT medium, see Supplementary Table 2) was added and plates transferred to humidified 37 °C/5% CO<sub>2</sub> incubators. In some cases, 25 ng ml<sup>–1</sup> HGF (Peprotech) was added to the medium (Supplementary Table 3). Medium was changed every 3–4 d and organoids were passaged every 1–4 weeks. Organoid passaging: organoids were mechanically sheared through P1000 pipet tip connected to P200 pipet tip without a filter. Dense organoids that were not easily sheared mechanically were collected with 1 ml pre-warmed (37 °C) Accutase solution (A6964, Sigma), incubated for 1–5 min at room temperature and mechanically sheared as before. Following the addition of 10 ml AdDF+++ and centrifugation at 1,200 r.p.m., organoid fragments were resuspended in cold BME and reseeded as above at suitable ratios (1:1 to 1:4) allowing the formation of new organoids. In some lines, organoids repeatedly appeared floating in medium. These organoid lines could be transferred to repellent plates (Greiner, 662970) and expanded with medium containing 5% BME (Supplementary Table 3).

Genetically manipulated FT clones were expanded in OCwnt medium.

**Scanning electron microscopy.** To remove BME, organoids were collected with Cell Recovery Solution (Corning) and gently shaken using tube rotator, for 30 min at 4 °C. Organoids were allowed to settle down with gravity, the recovery solution was removed and 1 ml of 1% (v/v) glutaraldehyde (Sigma) in PBS was added. Following an overnight fixation at 4 °C, organoids were transferred onto 12 mm poly-L-lysine coated coverslips (Corning). The organoids were serially dehydrated by consecutive 10 min incubations in 2 ml of 10% (v/v), 25% (v/v) and 50% (v/v) ethanol-PBS, 75% (v/v) and 90% (v/v) ethanol-H<sub>2</sub>O (2x) followed by 50% ethanol-hexamethyldisilazane (HMDS) and 100% HMDS (Sigma). Coverslips were removed from the 100% HMDS, air dried overnight at room temperature and mounted onto 12 mm specimen stubs (Agar Scientific). Following gold coating to 1 nm using a Q150R sputter coater (Quorum Technologies) at 20 mA, samples were examined with a Phenom PRO table-top scanning electron microscope (Phenom-World)

**Histology and imaging.** Tissue and organoids were fixed in 4% paraformaldehyde followed by dehydration, paraffin embedding, sectioning and standard HE

staining. For the blind test, sections were randomized and analyzed by an OC pathologist. Immunohistochemistry was performed using antibodies as specified in Supplementary Table 9.

Images were acquired on a Leica Eclipse E600 microscope and processed using the Adobe Creative Cloud software package.

For time-lapse imaging, organoids were plated in BME in glass-bottom 96-well plates and mounted on an inverted confocal laser scanning microscope (Leica SP8X), which was continuously held at 37 °C and equipped with a culture chamber for overflow of 6.0% CO<sub>2</sub>. Over 16–20 h, approximately 10 H2B-mNeon-expressing organoids were imaged simultaneously in XYZT-mode using a ×40 objective (NA 1.1), using minimal amounts of 506 nm laser excitation light from a tunable white light laser. Images were taken at 4 min intervals.

**Genomic analysis.** For karyotyping, 0.1 μg ml<sup>–1</sup> colcemid (Gibco, 15212012) was added to the complete growth medium. About 12 h later organoids were harvested, trypsinized into single cells, incubated in hypotonic 75 mM KCl solution for 10 min and fixed in methanol:acetic acid solution (3:1). Metaphase spreads were prepared, mounted with DAPI-containing Vectashield, imaged on a DM6000 Leica microscope and quantified by manual chromosome counting. A minimum of 14 spreads was analyzed for each line.

For DNA isolation, library preparation and WGS, organoid and blood samples were processed by using the DNeasy Qiagen kit. DNA from tumor tissue was isolated with the Genomic Tip Qiagen kit, supplemented with RNase treatment. Quality and quantity of samples were checked with Qubit (DNA BR). DNA integrity and RNA contamination was assessed by using TapeStation DNA screens (Genomic screen) and Nanodrop (260/280 ratio).

Per sample, 500–1,000 ng of DNA was used for DNA library preparation, and whole-genome paired-end sequencing (2 × 150 bp) was performed on Illumina HiSeq X Ten and NovaSeq 6000 to an average coverage of 42x.

Supplementary Table 10 provides a list of all commercial and custom code used for data collection and analysis including: name, version, source and link.

WGS data were processed using our in-house Illumina Analysis Pipeline (IAP) v. 2.5.1 (<https://github.com/UMCUGenetics/IAP>). Briefly, reads were mapped against the human reference genome GRCh37 using Burrows–Wheeler Alignment with maximal exact matches (BWA-MEM), v. 0.7.5a-r405 (ref. <sup>58</sup>). Read mapping was followed by marking of duplicates, and indel-realignment, according to best practice guidelines<sup>59</sup> by the Genome Analysis ToolKit (GATK) v.3.4-46 (ref. <sup>60</sup>).

Normal cell contamination in tumor and organoid samples was estimated in silico using PURPLE v. 2.14<sup>37</sup>.

Somatic SNVs and indels were called in the tumor and the organoids independently using the corresponding blood sample as a reference and four different tools: Strelka, v.1.0.14 (ref. <sup>61</sup>); VarScan, v.2.4.1 (ref. <sup>62</sup>); FreeBayes, v.1.0.2 (ref. <sup>63</sup>); and Mutect, v.1.1.7 (ref. <sup>64</sup>). The functional effect of the somatic SNVs and indels were predicted using SnpEff v.4.1 (ref. <sup>65</sup>). Tumor/organoid pair VCF files were then merged by selecting high-confidence SNVs and indels with a minimum alternative allele read depth of five in the tumor or ten in the organoids and called by at least two independent somatic callers in either of the samples. In addition, high-confidence SNVs that were only detected in either the tumor or the organoid sample of a pair were called in the corresponding sample (tumor or organoid) when supported by more than 5% of the reads covering that position.

CNV was detected for each sample independently using Control-FREEC, v. 7.2 (ref. <sup>66</sup>) and assuming a ploidy of 2. For sample HGS-6, a ploidy of 3 was assumed for the plots.

Structural variation calling was performed using Manta, v.0.29.5 (ref. <sup>67</sup>). For increased sensitivity, we ran Manta in the four available analysis types: single-sample, multi-sample, tumor-only and tumor-normal. When comparing SVs called in one of the tumor/organoid pairs with the matching sample, we inspected the output of the tumor-normal mode of the pertinent tumor/organoid sample with the results of the four calling modes for the matching tumor/organoid sample.

Somatic variant calling could not be performed for samples without matching reference DNA (CCC-1 and END-1). In these cases, germline variant calling was performed jointly for tumor and organoid samples using GATK's Haplotype Caller, v3.4-46 (ref. <sup>60</sup>). Germline calls were filtered against the Genome of the Netherlands (GoNL)<sup>68</sup> and the 1000 Genomes<sup>69</sup> and only variants with a predicted 'moderate' or 'high' effect (SnpEff v.4.1 (ref. <sup>65</sup>)) were kept. For SV calling of the CCC-1 and END-1 samples, the tumor-normal mode of Manta could not be used, but all other Manta variant calling workflows were performed (tumor-only, single-sample, multi-sample). To enrich for somatic SVs, only SVs larger than 10 Kb and not found in the GoNL or 1000 Genomes studies were considered for these two samples.

**Single-cell WGS library preparation.** Cells were sorted into 384-well plates with 5 μl of mineral oil (Sigma-Aldrich). After sorting cells, can be stored at –20 °C. Five-hundred nanoliters of lysis mix (0.001 U μl<sup>–1</sup> Qiagen Protease in NEB Buffer 4) was added to each well and lysis was performed at 55 °C overnight followed by heat inactivation for 20 min at 75 °C and for 5 min at 80 °C. Five-hundred nanoliters of Restriction Enzyme mix (1 U μl<sup>–1</sup> NLAIII in NEB Cutsmart buffer) was added to each well and restriction was performed for 3 h at 37 °C followed by heat inactivation for 20 min at 65 °C. One-hundred nanoliters of 1 μM barcoded

double-stranded NLAIII adapter was added to each well. Ligation mix (1,100  $\mu$ l, 182 U  $\mu$ l<sup>-1</sup> T4 DNA Ligase in 1x T4 DNA Ligase buffer supplemented with 3 mM ATP) was added to each well and ligation was performed overnight at 16 °C. After ligation, single cells were pooled and library preparation was performed as described in Muraro et al.<sup>70</sup>. Libraries were sequenced on an Illumina Nextseq500 with 2 × 75-bp paired-end sequencing.

**Single-cell WGS data analysis.** Reads were aligned to GRCh38 using Burrows–Wheeler Aligner v0.7.14 mapping tool with settings 'bwa mem -M'<sup>71</sup>. Data were binned in 1 MB bins and normalized to the expected NLAIII mappability per bin. The expected NLAIII mappability per bin was calculated by generating 10<sup>8</sup> reads from the reference genome, with every read starting at a NLAIII site. These reads were subsequently mapped and binned using the same procedure as for the experimental data. The number of reads per bin was then divided by the average number of reads per bin to acquire the expected NLAIII mappability for each bin. Regions where the expected NLAIII mappability was <0.9 or >1.2 were excluded from further analysis. After this the cells were filtered and only cells with >20,000 reads were kept for further analysis. The median read count of each cell was then set to 2 to represent a diploid genome. Data were log<sub>2</sub> transformed to obtain log<sub>2</sub> CN ratios and smoothed using a running mean (R package caTools) with a width of 20 MB. To remove additional low-quality cells, the variance across the genome was calculated for each cell and cells with a variance >0.3 were removed. For two-dimensional visualization of the data, we first performed independent component analysis (ICA) (R package fastICA) followed by *t*-stochastic neighbor embedding (*t*-SNE) (R package Rtsne). Clustering was performed using ward.D2 hierarchical clustering on the Manhattan distances of the ICA-transformed data. Subsequently, the average copy number profile per cluster was calculated using the R package DNACopy. Finally, a tree was constructed using ward.D2 hierarchical clustering on the Manhattan distances of the DNACopy-derived CNV profiles of the non-diploid clusters.

**RNA-seq analysis.** RNA was isolated from organoids with Trizol Reagent (Ambion). RNA libraries were generated with the Truseq Stranded Ribo-zero Sample preparation kit. RNA integrity was assessed by TapeStation (RNA screen) and quantified by Qubit (RNA). Libraries were multiplexed and paired-end sequenced (2 × 75 bp) on Illumina NextSeq.

Supplementary Table 10 provides a list of all commercial and custom code used for data collection and analysis including: name, version, source and link.

RNA-seq data were processed with our in-house RNA analysis pipeline (v.2.3.0, <https://github.com/UMCUGenetics/RNASeq>). Reads were aligned to the human reference genome GRCh37 using STAR v. 2.4.2 (ref. <sup>72</sup>), and then read count was performed with HTSeq-count, v. 0.6.1 (ref. <sup>73</sup>). Features (ENSEMBL definitions GRCh37, release 74) with zero read counts were filtered out (21,711 features out of 63,677). Gene symbols were mapped to the ENSEMBL features using the biomaRt package v. 2.26.1 (ref. <sup>74</sup>), and features without corresponding gene symbols and with duplicate mappings were removed. The final count matrix consisted of 30,080 rows (genes). The DESeq2 package, v1.10.1 (ref. <sup>75</sup>) was then used to normalize the read counts using the median-of-ratios method. Spearman correlation between samples was calculated using the normalized read counts from all 5,000 most-variable genes and samples were clustered using hierarchical clustering with complete linkage on the correlation matrix. The genetically modified organoid lines were analyzed using the same DESeq2 pipeline.

**Methylation analysis.** For methylation analysis 210 ng of genomic DNA was used. DNA was sodium bisulfite converted with the Zymo Research EZ DNA methylation kit (Zymo Research) and treated with the InfiniumHD FFPE Restore kit (Illumina). Next, the DNA was hybridized to the Infinium MethylationEPIC 850 K BeadChip (Illumina) to analyze the genome-wide methylation status of 865,859 methylation sites.

Supplementary Table 10 provides a list of all commercial and custom code used for data collection and analysis including: name, version, source and link.

For methylation data analysis, fluorescence intensity data (.IDAT) files were analyzed by using the minfi R package<sup>76</sup>. Beta-values were extracted after applying a normalization step with minfi preprocessFunnorm. Pearson correlation of beta-values between samples was calculated, and subsequently unsupervised hierarchical clustering of correlation values was performed on the 11,720 most variable probes.

**Gene editing.** Organoids derived from early passaged (P0–P3) FT organoids were dissociated into small clumps using pre-warmed Accutase solution (A6964, SIGMA), washed once with AdDF+++ and twice with Opti-MEM (11058021, Life technologies). Cells were suspended with 100  $\mu$ l Opti-MEM containing RHO/ROCK pathway inhibitor (10  $\mu$ M) and 10  $\mu$ g of pSpCas9(BB)-2A-GFP (a gift from F. Zhang<sup>77</sup> from the Broad Institute of Massachusetts Institute of Technology (MIT) and Harvard, Cambridge, MA, USA), Addgene plasmid no. 48138) with guide RNA (gRNA) targeting *TP53* (GACGGAAACCGTAGCTGCC)<sup>30</sup> or combination of gRNA targeting *TP53* and *RBI1* (GTTTCGAGGTGAACCATTAAT) genes, and transferred into 2 mm gap NEPA electroporation cuvette (lot no. 2S1509). For electroporation, we utilized NEPA21 type-II electroporator (Supplementary Table 11).

Following electroporation, 300  $\mu$ l of complete growth medium was added to the cells and they were incubated at room temperature for 15 min. Cells were centrifuged, suspended in 200  $\mu$ l BME and plated as previously described. Complete medium was added after cell BME suspension drops had solidified. Two to three days after electroporation, 10  $\mu$ M nutlin-3 (Cayman Chemical) was added to the growth medium. Two to three weeks after electroporation, single organoids were picked and transferred into 1.5 ml microcentrifuge tubes containing 200  $\mu$ l of pre-warmed Accutase. Following 2–3 min incubation, organoids were sheared into small cell clumps by pipetting, washed with 1 ml AdDF+++ and centrifuged for 5 min at 2,000 r.p.m. Cells were resuspended with 40  $\mu$ l BME and plated. For genotyping, genomic DNA was isolated using Viagen Direct PCR (Viagen). GoTaq Flexi DNA polymerase (Promega) was used for PCR amplification. Primer sequences: P53\_for, 5'-CAGGAAGCCAAAGGGTGAAGA-3'; P53\_rev, 5'-CCCATCTACAGTCCCCCTTG-3'; RBI\_for, 5'-CAGAGTAGAAGAGGG ATGGCA-3'; RBI\_rev, 5'-CAGTGATTCCAGAGTGACGGA-3'. Products were cloned into pGEM-T Easy vector system I (Promega) and sequenced using T7 sequencing primer.

**Lentivirus transduction of organoids.** To visualize mitoses, organoids were infected with lentivirus encoding mNeon-tagged histone-2B and a puromycin-resistance cassette (pLV-H2B-mNeon-ires-Puro<sup>50</sup>) as previously described<sup>78</sup>.

**Drug screen and viability assay.** Dispase II (1 mg ml<sup>-1</sup>; Invitrogen) was added to the medium of the organoids and these were incubated for 10 min at 37 °C to digest the BME. Subsequently, organoids were mechanically dissociated by pipetting and were filtrated using a 70 mm nylon cell strainer (Falcon), resuspended in 2% BME/growth medium (15,000–20,000 organoids ml<sup>-1</sup>) before plating in 50  $\mu$ l volume (Multi-drop Combi Reagent Dispenser) on BME pre-coated 384-well plates.

The drugs and their combinations were added 1 h after plating the organoids using the Tecan D300e Digital Dispenser. Drugs were dispensed in a randomized manner and DMSO end concentration was 1% in all wells. 120 h after adding the drugs, ATP levels were measured using the Cell-Titer Glo2.0 (Promega BV) according to the manufacturer's instructions and luminescence was measured using a SpectraMax microplate reader (Molecular Devices). Results were normalized to vehicle (DMSO = 100%) and baseline control (navitoclax 20  $\mu$ M).

Data were analyzed using GraphPad Prism 6. Using the trapezoid rule for numerical integration, the AUC was approximated between the lowest and highest concentrations screened in the actual assay. Organoid drug sensitivity was represented by the average AUC of two technical replicates and independent experimental repetitions in a subset of treatments and visualized using RStudio. Experimental repetition with a subset of drugs was performed in the following lines: FT-1, FT(P)-1, END-1.1, END-1.2, MC-2.1, HGS-1, HGS-1-R2, HGS-3.1, HGS-3.2, HGS-22, HGS-23. Euclidean distance between samples was measured using the normalized (row Z-score) AUC.

Alpelisib (BYL719), catalog no. S2814, Selleckchem; adavosertib (MK-1775), catalog no. S1525, Selleckchem; AZD8055, catalog no. S1555, Selleckchem; carboplatin, catalog no. S1215, Selleckchem; gemcitabine, catalog no. S1714, Selleckchem; MK-2206, catalog no. S1078, Selleckchem; niraparib (MK-4827), catalog no. S2741, Selleckchem; nutlin-3, catalog no. 10004372, Cayman Chemical; paclitaxel, catalog no. S1150, Selleckchem; pictilisib (GDC-0941), catalog no. S1065, Selleckchem.

**RECAP assay.** Organoids were incubated at 37 °C/5% CO<sub>2</sub> humidified atmosphere and an equal number of organoids were transferred to 3 cm Petri dishes containing 2 ml of medium. One petri dish was irradiated with 5 Gy X-rays (200 kV, 4 mA, YXLON Y.TU 225-D02) and the other Petri dish was mock-treated (that is not irradiated). EdU (0.02 mM; ThermoFisher Scientific, Click-iT EdU Alexa Fluor 647 Imaging Kit, catalog no. C10340) was added to the organoids and incubated for 2 h at 37 °C/5% CO<sub>2</sub> humidified atmosphere on a 60 r.p.m. rotating platform. The organoids were transferred to 15 ml falcon tubes and after the organoids were settled down by normal gravity at room temperature, medium was removed and replaced by 10 ml buffered formalin (10%). Organoids were fixed for 1 h on a rotating device at room temperature, washed twice with PBS and stored in 70% ethanol at 4 °C. The organoids were embedded into paraffin, sliced into 5  $\mu$ m slices and incubated in 60 °C o/n on StarFrost microscope slides (76 × 26 mm, Knittel glass). Immunofluorescence staining was performed to stain for DAPI (ThermoFisher Scientific, catalog no. P36935), geminin (primary antibody rabbit, Proteintech Europe, catalog no. 10802-1-AP), RAD51 (primary antibody mouse, Gene Tex, GTX70230) and EdU (ThermoFisher Scientific, Click-iT EdU Alexa Fluor 647 Imaging Kit, catalog no. C10340). RAD51 foci were scored blindly in 10 randomly chosen organoids, counting at least 100 geminin<sup>+</sup> cells in total for both the irradiated and the non-irradiated organoids. Biological repetitions were done as indicated in figure legend (Fig. 6). A nucleus was scored as RAD51 positive if it contained more than five foci. Organoids in which less than six cells were counted as geminin<sup>+</sup> were filtered out from the analysis.

**Organoid-derived xenograft.** Experiments on NSG mice were carried out at the Netherlands Cancer Institute according to local and international regulations and ethical guidelines, and were approved by the local and central animal experimental

committee at the Netherlands Cancer Institute (AVD3010020172464; IVD 9.1 EGP 8102) 8102)

Ovarian injection: mice were anesthetized with isoflurane (3% induction, and 2% maintenance) and a small incision in the flank and peritoneum was made.

The ovary was gently taken from the abdominal cavity and tumor cells are slowly injected with an insulin needle (Terumo 29 G x ½, 0.33 × 12 mm) into the bursa. The ovary was positioned back in the abdominal cavity, and peritoneum and skin were sutured separately.

IVIS-imaging: mice were injected with 10 µl per g body weight of Beetle luciferin (promega E1605) and after 10 min bioluminescence was measured on the IVIS Lumina. After the mice were killed, the ovary was taken out and embedded in paraffin for further analysis.

Intervention study: experiments on NSG mice were carried out at the Netherlands Cancer Institute according to local and international regulations and ethical guidelines, and were approved by the local animal experimental committee at the Netherlands Cancer Institute (AVD301002015407; IVD 1.1 EGP 8583).

Subcutaneous injection: mice are subcutaneously injected with the organoid lines. Caliper measurements were performed three times per week. When the tumors reached a size of 50 mm<sup>3</sup>, treatment started with either Vehicle (saline) or Gemcitabine (2 mg/kg), intraperitoneal injection 5 times per week (5 on, 2 off) for 4 consecutive weeks. Ten mice per treatment arm were included. Tumor size was monitored for 55 d; mice that died before that time point (after surgery or gemcitabine treatment) were excluded from the analysis.

**Statistical analyses.** Where applicable, statistical methods are outlined in the respective figure legends.

Statistical analysis was performed utilizing Microsoft Excel, GraphPad and R package.

P values were calculated using a two-tailed Student's *t*-test. DNA and RNA sequencing analysis details can be found in the relevant Methods sections.

For karyotyping a minimum of 14 metaphase spreads was analyzed for each line. For single-cell DNA analysis 791 cells from 2 recurrent tumor samples and 3 corresponding organoid lines were analyzed. Drug screen killing curves show the average ± s.e.m. of two technical replicates. AUC of independent drug screen repetitions was averaged and presented in drug sensitivity heat map (experimental repetitions (*n* = 2) at different passage number in a subset of treatments was carried out in 11 independent organoid lines, Extended Data Fig. 5d). For animal intervention experiments, 10 mice per treatment arm were included. Mice that died before the experimental end-point were excluded from analysis. In the case of representative results, the number of independent organoid lines or experimental repetitions and their relevant description are indicated in the figure legend.

**Clinical data.** Patients agreed with the use of their clinical data by signing informed consent. Clinical data was extracted from the patient file by the Dutch Cancer Registration and included age at diagnosis, patient history, *BRCA* mutation status, tumor characteristics and treatment modalities.

**Reporting Summary.** Further information on research design is available in the Nature Research Reporting Summary linked to this article.

### Data availability

BAM files for DNA and RNA sequencing data are made available through controlled access at the European Genome-phenome Archive (EGA) which is hosted at the EBI and the CRG (<https://ega-archive.org>), under accession number EGA: EGAS00001003073. Data access requests will be evaluated by the UMCU Department of Genetics Data Access Board (EGAC00001000432) and transferred on completion of a material transfer agreement and authorization by the medical ethical committee UMCU at request of the HUB to ensure compliance with the Dutch 'medical research involving human subjects' act.

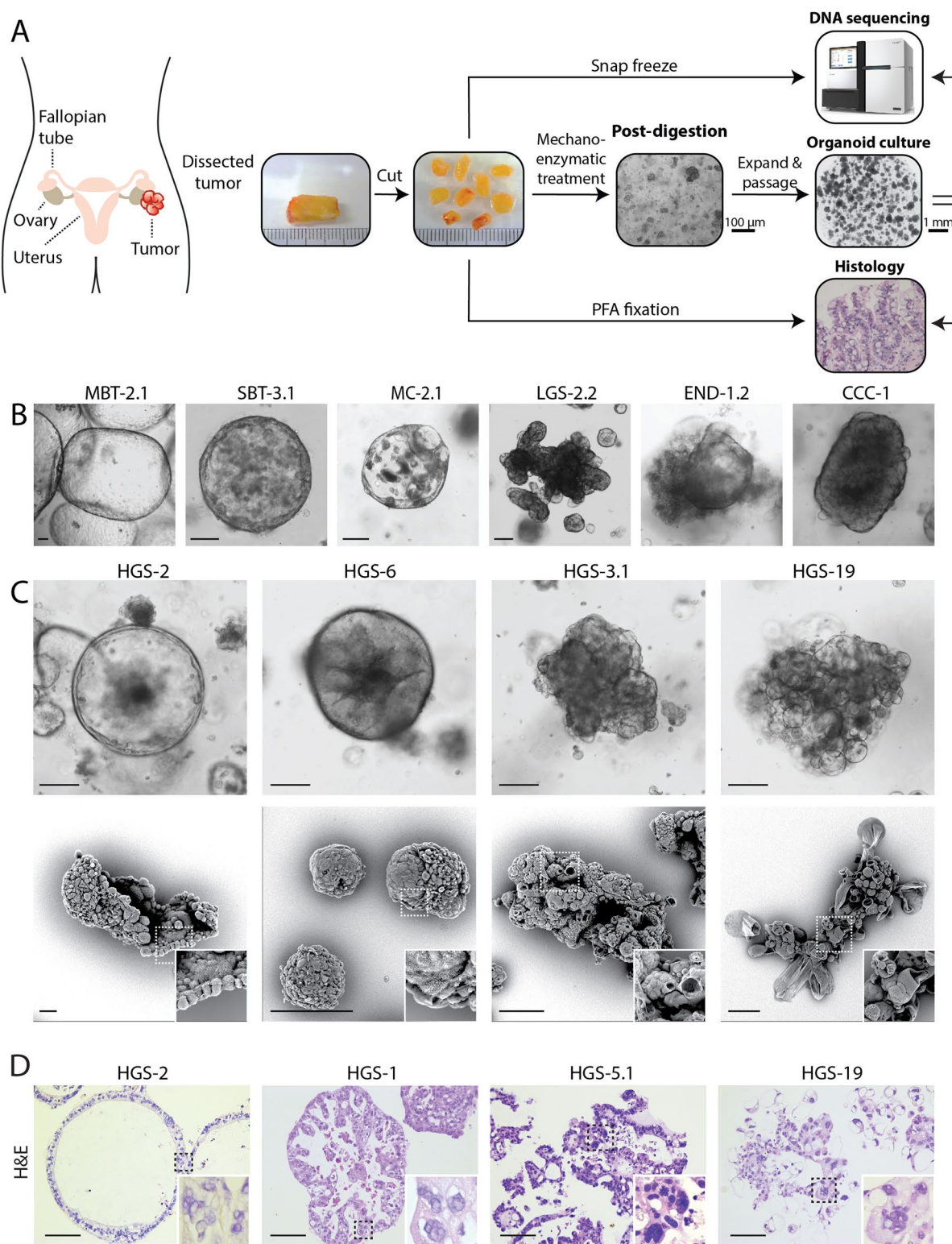
### Code availability

Illumina data processing pipeline v2.2.1 is available at <https://github.com/UMCUGenetics/IAP/releases/tag/v2.2.1> and RNA analysis pipeline v2.3.0 is available at <https://github.com/UMCUGenetics/RNASeq>. All other custom code used for this study is available at <https://github.com/UMCUGenetics/OvCaBiobank>

### References

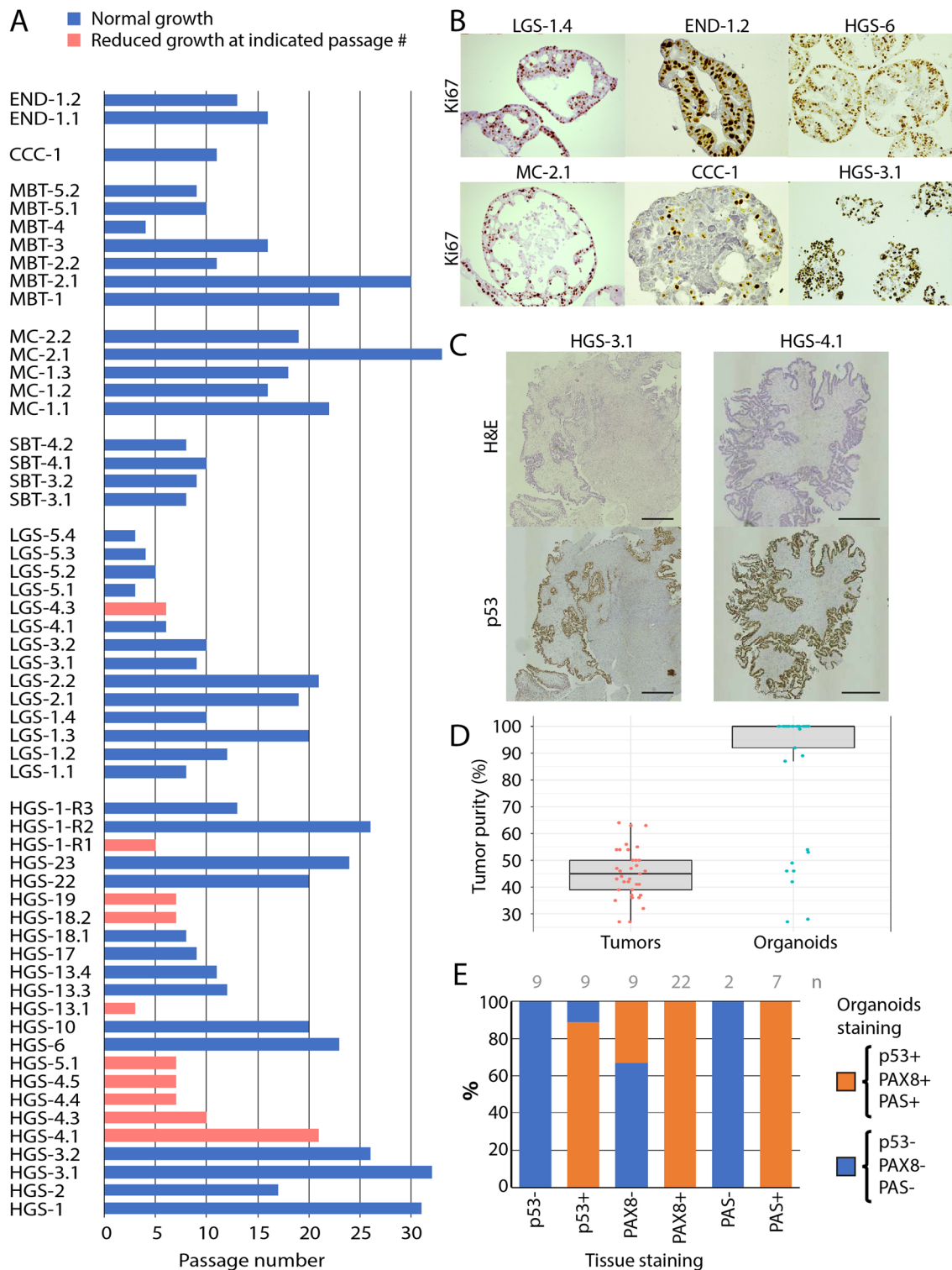
- Li, H. Aligning sequence reads, clone sequences and assembly contigs with BWA-MEM. Preprint at <https://arxiv.org/abs/1303.3997> (2013).
- Van der Auwera, G. A. et al. From FastQ data to high confidence variant calls: the Genome Analysis Toolkit best practices pipeline. *Curr. Protoc. Bioinformatics* **43**, 11.10.1–11.10.33 (2013).
- McKenna, A. et al. The genome analysis toolkit: a MapReduce framework for analyzing next-generation DNA sequencing data. *Genome Res.* **20**, 1297–1303 (2010).
- Saunders, C. T. et al. Strelka: accurate somatic small-variant calling from sequenced tumor-normal sample pairs. *Bioinformatics* **28**, 1811–1817 (2012).
- Koboldt, D. C. et al. VarScan 2: somatic mutation and copy number alteration discovery in cancer by exome sequencing. *Genome Res.* **22**, 568–576 (2012).
- Garrison, E. & Marth, G. Haplotype-based variant detection from short-read sequencing. Preprint at <https://arxiv.org/abs/1207.3907> (2012).
- Cibulskis, K. et al. Sensitive detection of somatic point mutations in impure and heterogeneous cancer samples. *Nat. Biotechnol.* **31**, 213–219 (2013).
- Cingolani, P. et al. A program for annotating and predicting the effects of single nucleotide polymorphisms, SnpEff: SNPs in the genome of *Drosophila melanogaster* strain w1118; iso-2; iso-3. *Fly (Austin)* **6**, 80–92 (2012).
- Boeva, V. et al. Control-FREEC: a tool for assessing copy number and allelic content using next-generation sequencing data. *Bioinformatics* **28**, 423–425 (2012).
- Chen, X. et al. Manta: rapid detection of structural variants and indels for germline and cancer sequencing applications. *Bioinformatics* **32**, 1220–1222 (2016).
- The Genome of the Netherlands Consortium. Whole-genome sequence variation, population structure and demographic history of the Dutch population. *Nat. Genet.* **46**, 818–825 (2014).
- Genomes Project, C. et al. A global reference for human genetic variation. *Nature* **526**, 68–74 (2015).
- Muraro, M. J. et al. A single-cell transcriptome atlas of the human pancreas. *Cell Syst.* **3**, 385–394.e3 (2016).
- Li, H. & Durbin, R. Fast and accurate short read alignment with Burrows-Wheeler transform. *Bioinformatics* **8**, 1754–1760 (2009).
- Dobin, A. et al. STAR: ultrafast universal RNA-seq aligner. *Bioinformatics* **29**, 15–21 (2013).
- Anders, S., Pyl, P. T. & Huber, W. HTSeq—a Python framework to work with high-throughput sequencing data. *Bioinformatics* **31**, 166–169 (2015).
- Durinck, S. et al. Mapping identifiers for the integration of genomic datasets with the R/Bioconductor package biomaRt. *Nat. Protoc.* **4**, 1184–1191 (2009).
- Love, M. I., Huber, W. & Anders, S. Moderated estimation of fold change and dispersion for RNA-seq data with DESeq2. *Genome Biol.* **15**, 550 (2014).
- Aryee, M. J. et al. Minfi: a flexible and comprehensive Bioconductor package for the analysis of Infinium DNA methylation microarrays. *Bioinformatics* **30**, 1363–1369 (2014).
- Ran, F. A. et al. Genome engineering using the CRISPR–Cas9 system. *Nat. Protoc.* **8**, 2281–2308 (2013).
- Koo, B. K. et al. Controlled gene expression in primary Lgr5 organoid cultures. *Nat. Methods* **9**, 81–83 (2011).

## Extended Data Fig. 1 - Derivation and morphological differences of OC organoids



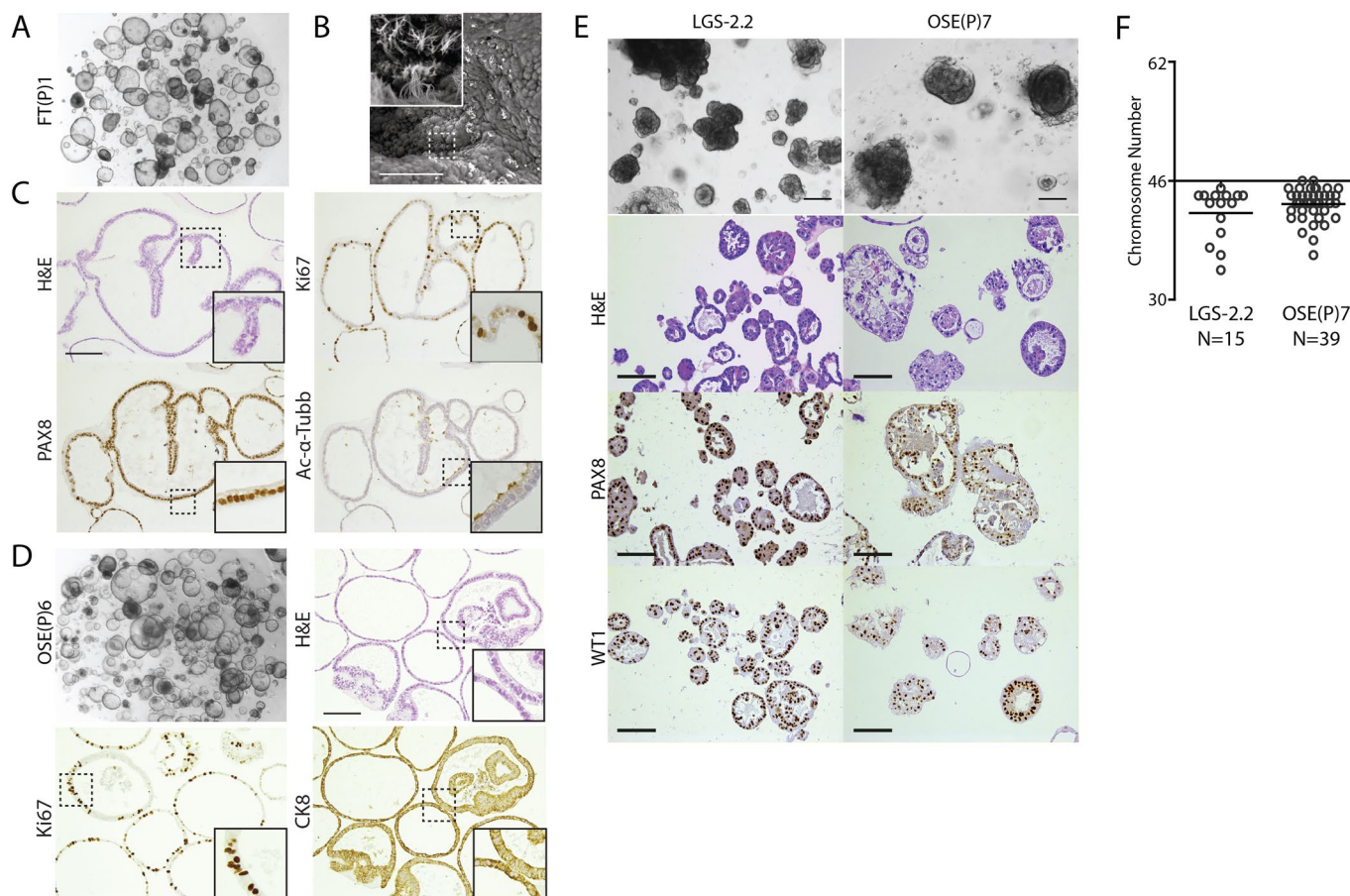
**Extended Data Fig. 1 | Derivation and morphological differences of OC organoids.** **a**, Schematic of OC organoid derivation. **b**, Bright-field images of MBT, SBT, MC, LGS, END and CCC organoids (left to right), depicting different organoid morphologies. Morphological description of 50 independent organoid lines is provided in Supplementary Table 6. Scale bar, 100  $\mu$ m. **c**, Bright-field (top) and SEM (bottom) images demonstrating main morphologies among different HGS organoid lines. Starting with cystic and well-organized cellular polarity, where microvilli are directed toward the organoid lumen (most left) to dense organoids that gradually (from left to right) show reduced circularity and cellular cohesiveness up to a grape-like shape morphology (most right). Scale bar, 100  $\mu$ m. **d**, High-magnification H&E staining images displaying representative examples of HGS organoid morphologies as well as nuclear and cellular atypia, typically displayed by HGS tumors. Histological description of 50 independent organoid lines is provided in Supplementary Table 6. Scale bar, 100  $\mu$ m.

Extended Data 2- Organoid lines' overview and tumor purity



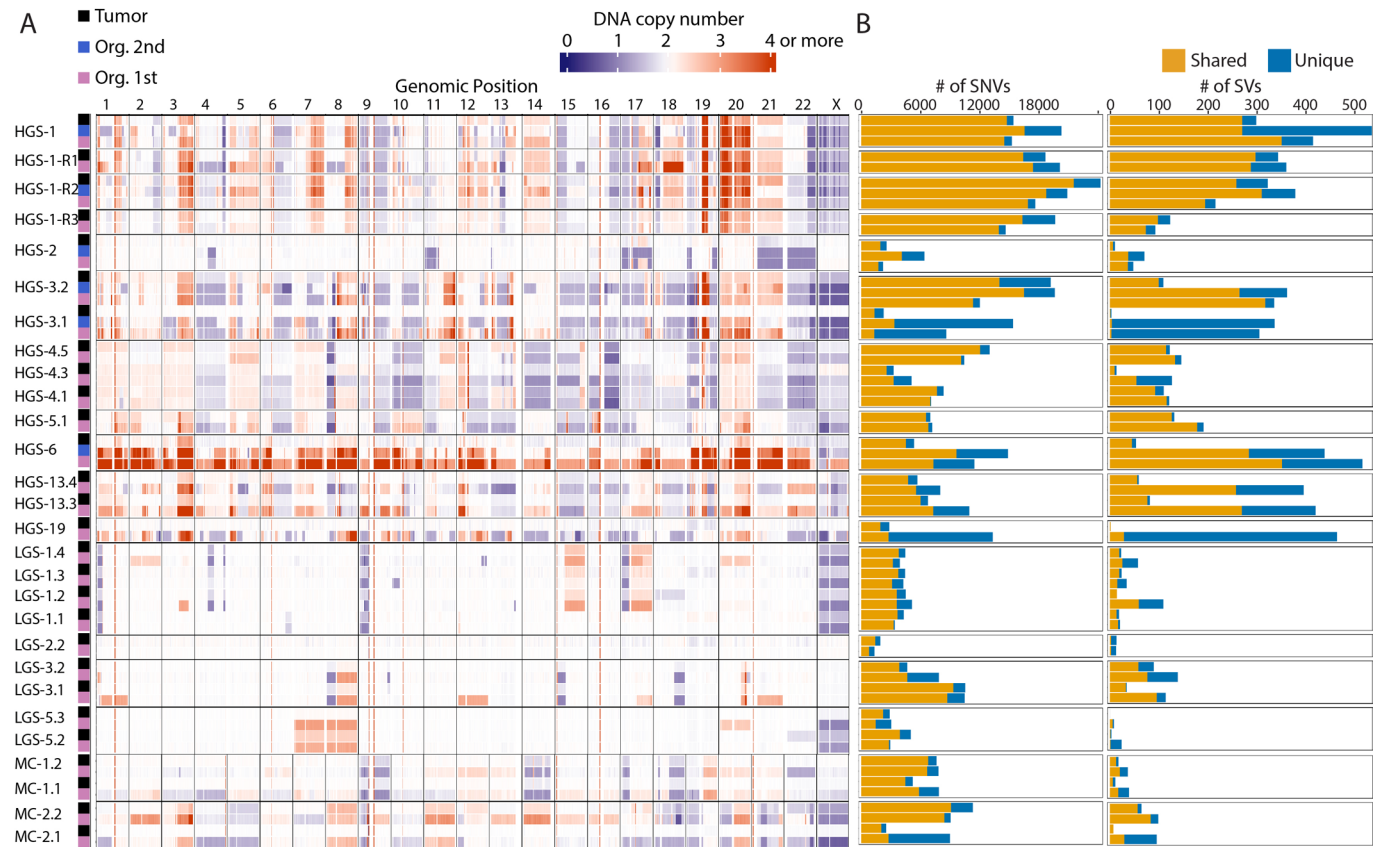
**Extended Data Fig. 2 | Organoid passage number overview and normal cell contamination in tumors and organoids.** **a**, Column bar graph depicting organoid maximum passage number up until the moment of submission. Organoids that stopped/slowed down their growth are indicated in orange. **b**, Representative images of Ki67 staining of six independent organoid lines show a high percentage of ki67-positive proliferating cells. **c**, Histological and immunohistochemical images of tumor tissue (derived from two independent patients) showing tumor cell purity within different samples, based on H&E and p53 staining. Scale bar, 0.5 mm. **d**, Tukey box-and-whisker plot (1.5x interquartile range) presenting bioinformatic estimation of tumor cell purity percentage of both tissue (n=35) and organoid (n=36) based on WGS data using PURPLE. Horizontal bars represent median of all dots. Mean and standard deviation across all samples are as follows: 45±9.2% (tissue) and 88.1±23% (organoids). **e**, Stacked bar chart showing the percentage of organoid lines that are positive for p53, PAX8 and periodic acid-Schiff (PAS) staining (orange) and negative (blue) grouped per original tumor staining status (see also Supplementary Table 6). Total number (n) of tissues stained per group are indicated.

## Extended Data 3- FT and OSE organoids



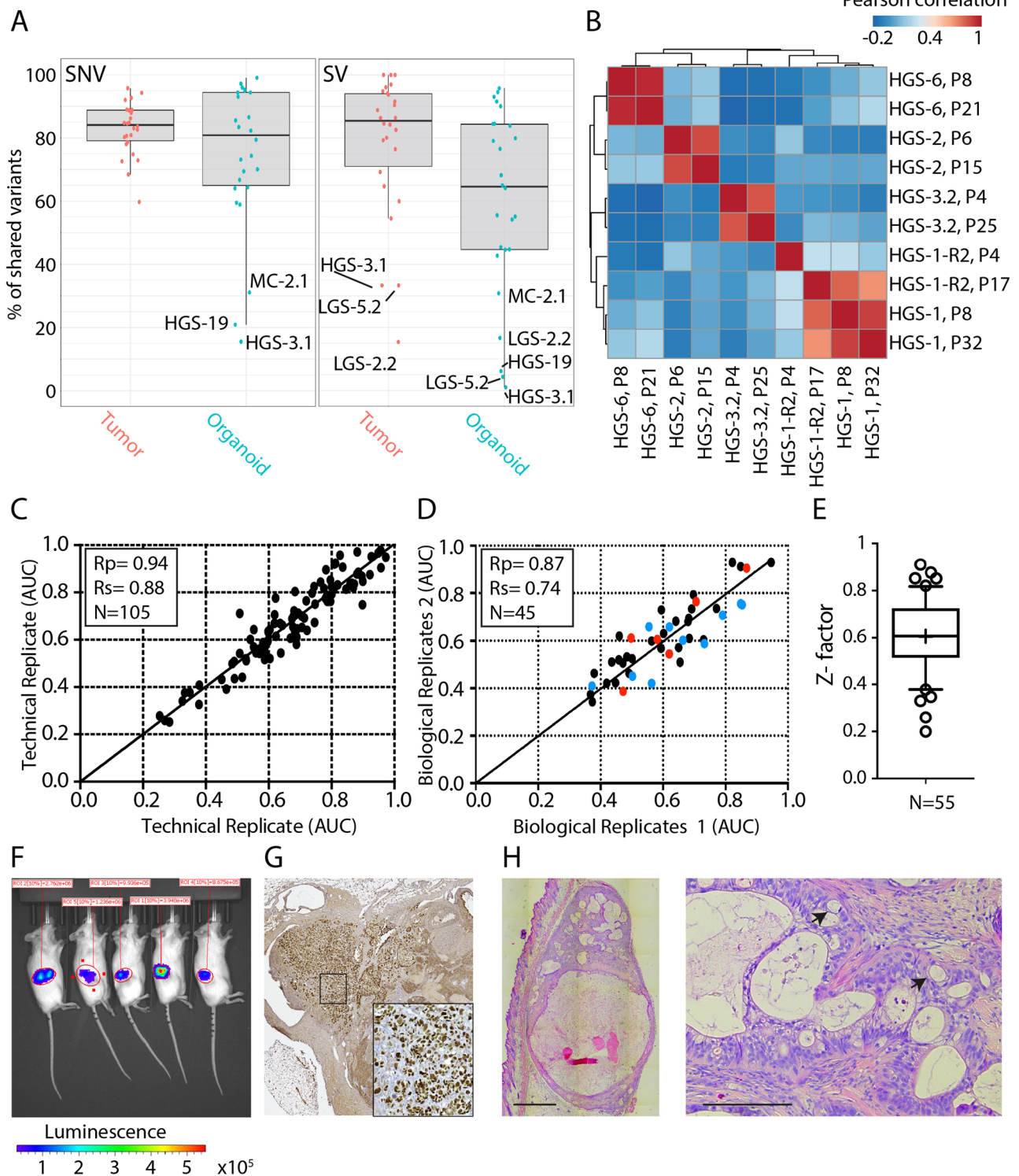
**Extended Data Fig. 3 | FT and OSE organoids.** **a**, An overview image of normal FT organoids embedded in 40  $\mu$ l BME drops, displaying a cystic morphology. All FT organoid lines that were established ( $n=22$ ) displayed cystic morphology. **b**, Representative SEM image showing ciliated cells facing FT organoid lumen. Scale bar, 50  $\mu$ m. SEM was performed on one FT organoid line. **c**, Histological analysis of FT organoids demonstrating H&E, Ki67, PAX8 and Ac- $\alpha$ -tubb staining. Histological analysis was performed on three independent FT organoid lines with similar results. Scale bar, 100  $\mu$ m. **d**, An overview image of normal OSE organoids embedded in 40  $\mu$ l BME drops displaying cystic morphology (top left image). Seven out of eight OSE organoid lines that were established displayed cystic morphology. OSE organoid images of H&E, Ki67 and cytokeratin 8 (CK8) staining, demonstrating a cystic morphology of proliferative epithelial cells. Histological analysis was performed on two independent OSE organoid lines with similar results. Scale bar, 100  $\mu$ m. **e**, First row: bright-field images of LGS-2.2 (left) and OSE(P)7 (right) organoid lines. Unlike normal FT and OSE that display cystic morphology both lines show dense phenotype. OSE(P)7 is the only OSE organoid line that display dense phenotype. Scale bar, 200  $\mu$ m. Second to last rows: histological and immunohistochemical images demonstrate that organoids are positively stained for PAX8 and WT1, markers of OC serous subtypes. Organoids display reduced cellular organization in comparison to normal FT and OSE organoids. Scale bar, 100  $\mu$ m. **f**, Scatter plot presenting metaphase spread analysis and mean for each line. Both lines present aneuploidy.

Extended Data 4- Genome wide tumor and organoid pair comparison



**Extended Data Fig. 4 | Genome-wide tumor and organoid pair comparison.** **a**, Genome-wide CNVs in tumor/organoid pairs (black, tumors; pink, organoids early passage; blue, organoids late passage) depicting gains (red) and losses (blue). **b**, Number of shared (yellow) and unique (blue) SNVs (on the left) and SVs (on the right) between tumor/organoid pairs. Shared variants are those that can be found in the corresponding paired sample. Passage number at which organoid lines were sequenced is given in Supplementary Table 7.

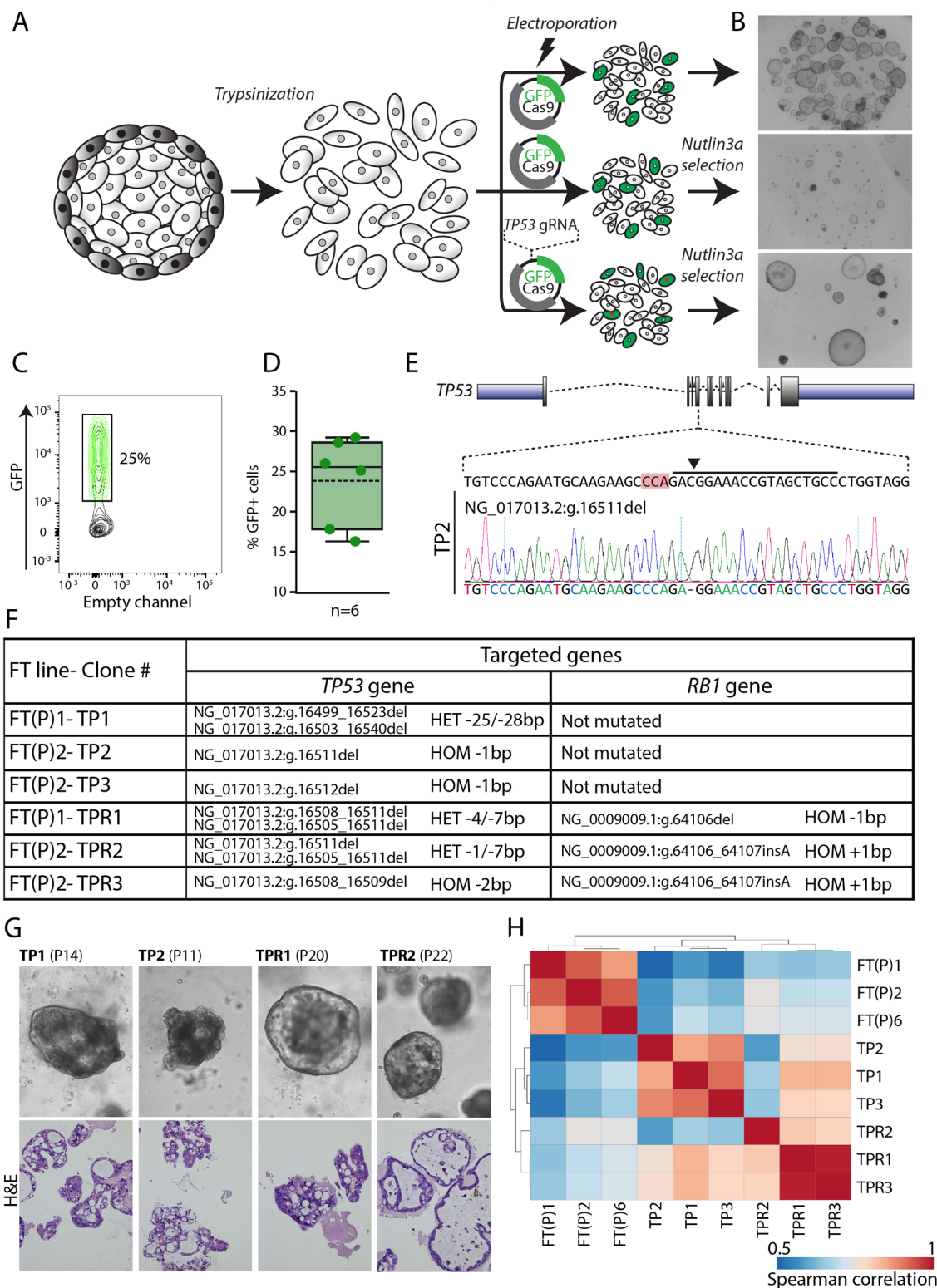
# Extended Data 5- Molecular characterization, drug screening and xenografts of OC organoids



Extended Data Fig. 5 | see figure caption on next page.

**Extended Data Fig. 5 | Molecular characterization, drug screening and xenografts of OC organoids.** **a**, Tukey box and whisker plot (1.5× interquartile range) summarizing the percentage of shared variants across all tumor (red) and organoid (green) samples. Right and left panels display SNVs and SVs, respectively. Horizontal bars represent median of all dots. Mean and standard deviation across all samples are as follows: SNVs,  $82.95 \pm 8.18\%$  (tissue,  $n = 31$ ) and  $75.62 \pm 23.13\%$  (organoids,  $n = 31$ ); SVs,  $78.14 \pm 22.11\%$  (tissue,  $n = 31$ ) and  $60.47 \pm 29.13\%$  (organoids,  $n = 31$ ). Samples with a low percentage of shared variants are indicated. **b**, Heat map of five independent organoid lines from both early and late passages based on 11,720 methylation probes. The heat map colors represent Pearson correlation values, as calculated from the methylation beta-values. Clustering of the correlation values was performed using hierarchical clustering based on complete linkage. **c**, Scatter plot of AUC values across all drug screening data, displaying high correlation between technical replicates (Pearson correlation = 0.94,  $R^2 = 0.88$ ,  $n = 105$ ). **d**, Scatter plot of AUC values of biological replicates, displaying high correlation (Pearson correlation = 0.87,  $R^2 = 0.74$ ,  $n = 45$ ). Colored dots represent biological replicates in which passage differences between experimental repetition is as follows: 1–2 passages,  $n = 29$  (black); 3–5 passages,  $n = 10$  (blue) and 13–22 passages,  $n = 6$ , (red), demonstrating stable drug sensitivity even after prolonged passaging. **e**, Box-and-whisker plot (10th–90th percentile) showing Z-factor distribution and mean across all drug screening plates. Mean = 0.61, ranging between 0.2 and 0.91,  $n = 55$ . **f**, Bioluminescence imaging of mice, orthotopically transplanted with luciferase expressing organoid lines depicting tumor growth. A summary of organoid-derived xenograft experiments is presented in Supplementary Table 8. **g**, p53 staining of organoid-derived xenograft (HGS-3.1) on orthotopic transplantation into the mouse bursa shows p53 overexpression in tumor cells. **h**, Histological analysis of an organoid-derived xenograft (MC-2.1) on subcutaneous transplantation. H&E staining shows haphazardly arranged neoplastic glands lined by columnar cells with variable numbers of goblet cells (arrows), which are specific features of MC. A summary of organoid-derived xenograft experiments is presented in Supplementary Table 8. Left image scale bar, 1 mm. Right image scale bar, 200  $\mu\text{m}$ .

Extended Data 6- CRISPR-Cas9 mediated genetic manipulation in FT organoids



Extended Data Fig. 6 | see figure caption on next page.

**Extended Data Fig. 6 | CRISPR-Cas9 mediated genetic manipulation in FT organoids.** **a**, Schematic of normal FT organoid electroporation. FT organoids were dissociated into small cell clumps and electroporated with either an empty vector or a vector containing a gRNA directed against *TP53*. Cells were plated and after 2 d of recovery nutlin3a was added. **b**, Overview images of organoids 2 weeks after electroporation. Organoids that were electroporated with an empty vector and not treated with nutlin3a showed nice recovery following electroporation (top), whereas the growth of organoids electroporated in a similar manner was dramatically inhibited when nutlin3a was added (middle). Surviving clones that are not inhibited by nutlin3a treatment are visible only when organoids were electroporated with a vector containing *TP53* gRNA (bottom). Four independent electroporation experiments followed by nutlin3A treatment were conducted giving rise to multiple Nutlin3A resistant clones. **c**, A representative flow cytometry analysis of organoids 48 h following electroporation demonstrating 25% of the cell express GFP. Summary of six independent repetitions of this experiment are presented in **d**. **d**, Box-and-whisker plot (minimum to maximum) showing the percentage of GFP positive cells following electroporation. Horizontal bars and dashed horizontal bars represent median and mean of all dots, respectively. Mean  $\pm$  s.d. =  $23.8 \pm 5.5\%$ , median = 25.5%. Six independent experiments that were conducted with three different FT organoid lines are presented, demonstrating high and robust electroporation efficiency. **e**, An example of CRISPR-Cas9 mediated editing of *TP53* gene in FT organoids. Targeted locus is presented and gRNA (solid line), PAM sequence (red highlight) and cut point (arrow head) are indicated. Sequencing results revealed out-of-frame deletions induced by CRISPR-Cas9 editing. **f**, Table presenting six FT genetically engineered clones derived from two independent donors (FT(P)1 and FT(P)2). For each clone, targeted gene description (in both *TP53* and *RB1* genes) including HGVS nomenclature is presented. (HET, heterozygous; HOM, homozygous). **g**, BF images (top) and H&E staining (bottom) of four independent clones show deviation from cystic and well-organized normal FT organoid morphology. Passage number is indicated. This analysis was conducted on three independent TP clones (loss-of-function mutations in the *TP53* gene) and three independent TPR clones (loss-of-function mutations in the *TP53* and *RB1* genes) with similar results. **h**, Heat map of Spearman correlation values of three independent normal FT organoid lines (derived from different donors) and genetically engineered clones ( $n = 3$  independent TP clones (loss-of-function mutations in the *TP53* gene) and 3 independent TPR clones (loss-of-function mutations in the *TP53* and *RB1* genes)), using RNA-seq expression data. Read counts were normalized for sequencing depth and the 1,000 most-variable genes were used. Clones were assigned into different groups according to their mutational profile.

## Reporting Summary

Nature Research wishes to improve the reproducibility of the work that we publish. This form provides structure for consistency and transparency in reporting. For further information on Nature Research policies, see [Authors & Referees](#) and the [Editorial Policy Checklist](#).

### Statistics

For all statistical analyses, confirm that the following items are present in the figure legend, table legend, main text, or Methods section.

n/a Confirmed

- The exact sample size ( $n$ ) for each experimental group/condition, given as a discrete number and unit of measurement
- A statement on whether measurements were taken from distinct samples or whether the same sample was measured repeatedly
- The statistical test(s) used AND whether they are one- or two-sided  
*Only common tests should be described solely by name; describe more complex techniques in the Methods section.*
- A description of all covariates tested
- A description of any assumptions or corrections, such as tests of normality and adjustment for multiple comparisons
- A full description of the statistical parameters including central tendency (e.g. means) or other basic estimates (e.g. regression coefficient) AND variation (e.g. standard deviation) or associated estimates of uncertainty (e.g. confidence intervals)
- For null hypothesis testing, the test statistic (e.g.  $F$ ,  $t$ ,  $r$ ) with confidence intervals, effect sizes, degrees of freedom and  $P$  value noted  
*Give  $P$  values as exact values whenever suitable.*
- For Bayesian analysis, information on the choice of priors and Markov chain Monte Carlo settings
- For hierarchical and complex designs, identification of the appropriate level for tests and full reporting of outcomes
- Estimates of effect sizes (e.g. Cohen's  $d$ , Pearson's  $r$ ), indicating how they were calculated

*Our web collection on [statistics for biologists](#) contains articles on many of the points above.*

### Software and code

Policy information about [availability of computer code](#)

Data collection

Supplementary table 9 provides a list of all commercial and custom code used for Data collection including: name, version, source and link. The following codes were used:  
Illumina Analysis Pipeline (IAP), BWA-MEM, Sambamba, FastQC, RNAseq pipeline, STAR, HTSeq-count

Data analysis

FlowJo, Microsoft Excel; GraphPad; R package; Python package  
Supplementary table 9 provides a list of all commercial and custom code used for Data analysis including: name, version, source, and link. The following codes were used:  
Illumina Analysis Pipeline (IAP), Picard, bamMetrics, Genome Analysis ToolKit (GATK), SnpEff/SnpSift, VCFtools, Strelka, VarScan, FreeBayes, MuTect, Vt, FreeC, Manta, IGVtools, Samtools, PURPLE, RNAseq pipeline, DESeq2 - R package, biomaRt - R package, pheatmap - R package, ggplot2 - R package, reshape2 - R package, ggrepel - R package, gtools - R package, gridExtra - R package, RColorBrewer - R package, Pysam - Python package, PyVCF - Python package, Miscellaneous

For manuscripts utilizing custom algorithms or software that are central to the research but not yet described in published literature, software must be made available to editors/reviewers. We strongly encourage code deposition in a community repository (e.g. GitHub). See the Nature Research [guidelines for submitting code & software](#) for further information.

### Data

Policy information about [availability of data](#)

All manuscripts must include a [data availability statement](#). This statement should provide the following information, where applicable:

- Accession codes, unique identifiers, or web links for publicly available datasets
- A list of figures that have associated raw data
- A description of any restrictions on data availability

BAM files for DNA and RNA sequencing data are made available through controlled access at the European Genome-phenome Archive (EGA) which is hosted at the EBI and the CRG (<https://ega-archive.org>), under accession number EGA: EGAS00001003073. Data access requests will be evaluated by the UMCU Department of

## Field-specific reporting

Please select the one below that is the best fit for your research. If you are not sure, read the appropriate sections before making your selection.

Life sciences  Behavioural & social sciences  Ecological, evolutionary & environmental sciences

For a reference copy of the document with all sections, see [nature.com/documents/nr-reporting-summary-flat.pdf](https://www.nature.com/documents/nr-reporting-summary-flat.pdf)

## Life sciences study design

All studies must disclose on these points even when the disclosure is negative.

Sample size	For obtaining organoid lines, no sample-size calculation was performed. Number of lines was derived from the number of patients that were recruited for the study and the efficiency rate of establishing organoid lines. Tissue was collected over the course of approximately one year. Organoid bio-bank size was derived from the number of recruited patients and organoid derivation efficiency. All lines that were included in this study were passaged at least 3 times. Efficiency of organoid derivation is the number of patients from which we established organoids divided by the total number of patients from which we received tissue (after derivation protocol was finalized). In some experiments, qualitative data were obtained (e.g. microscopy images of tumor versus normal) rather than quantitative. Summary of staining results for all lines that were tested is summarized in supplementary table 6 and Extended Data 2E. DNA, RNA and drug screening analysis was performed on available organoid lines that represent a wide variety of ovarian cancer subtypes.
Data exclusions	No data was excluded
Replication	For metaphase spread analysis at least 14 spreads were counted and in many cases more. WGS analysis was performed on 17 HGS, 9 LGS, 4 SBT, 4 MC and 3 MBT 1 CCC and 2 END organoid lines. Thus, providing a representative panel of all obtained subtypes. RNA analysis was conducted on 15 HGS, 10 LGS, 4 MC, 3 MBT, 1 CCC, 2 END and 6 normal samples. RNA analysis for genetic modified lines was done for 3 clones with TP53 mutation and 3 clones with both TP53 and RB1 mutations. clones were established from 2 donors. Drug screen experiments were done in technical duplication on 21 independent organoid lines. Independent drug screen repetitions (n=2) at different passage number in a subset of treatments was carried out in 11 independent organoid lines. Both technical and biological repetition were successful and demonstrated drug screen robustness. For intervention experiments we started with 20 mice (10 vehicle, 10 gemcitabine). For REcombination CAPacity (RECAP) assay a minimum of 100 cells were analyzed for each line. RAD51 score was included in the analysis only if a minimum number of 6 Geminin+ cells were counted in a given organoid.
Randomization	For histological analysis of organoids by a certified pathologist samples were randomized and blinded test was conducted For intervention experiments - When the tumors reached a size of 50 mm <sup>3</sup> mice were randomly selected and treated with intraperitoneal injections of Gemcitabine or vehicle.
Blinding	For WGS analysis (CNVs), RNA expression analysis and drug screen assays, the identity of ovarian cancer organoid subtypes was not known beforehand. For histological analysis of organoids by a certified pathologist samples were randomized and blindly analyzed. For REcombination CAPacity (RECAP) assay- The percentage of Geminin+ cells with RAD51 foci was scored blinded for sensitivity to Niraparib. Organoids that were analyzed were randomly selected.

## Reporting for specific materials, systems and methods

We require information from authors about some types of materials, experimental systems and methods used in many studies. Here, indicate whether each material, system or method listed is relevant to your study. If you are not sure if a list item applies to your research, read the appropriate section before selecting a response.

### Materials & experimental systems

n/a	Involved in the study
<input type="checkbox"/>	<input checked="" type="checkbox"/> Antibodies
<input checked="" type="checkbox"/>	<input type="checkbox"/> Eukaryotic cell lines
<input checked="" type="checkbox"/>	<input type="checkbox"/> Palaeontology
<input type="checkbox"/>	<input checked="" type="checkbox"/> Animals and other organisms
<input type="checkbox"/>	<input checked="" type="checkbox"/> Human research participants
<input checked="" type="checkbox"/>	<input type="checkbox"/> Clinical data

### Methods

n/a	Involved in the study
<input checked="" type="checkbox"/>	<input type="checkbox"/> ChIP-seq
<input type="checkbox"/>	<input checked="" type="checkbox"/> Flow cytometry
<input checked="" type="checkbox"/>	<input type="checkbox"/> MRI-based neuroimaging

## Antibodies

Antibodies used	Antibody, Company, Cat#, Dilution, Incubation, Antibody retrieval PAX8 Proteintech, 10336-1-AP 1:2000 Overnight, RT Citrate buffer, pH 6.0 (immunogene catalog number AG0306)
-----------------	--

p53 Santa Cruz, sc-6243 1:500 Overnight, RT Citrate buffer, pH 6.0 (Clone number- FL-393)  
 WT1 Abcam, Ab89901 1:300 Overnight, RT Tris/EDTA, pH 9.0 (Clone number- CAN-R9(IHC)-56-2)  
 Ki67 Monosan 1:2000 Overnight, RT Citrate buffer, pH 6.0  
 Ac-alpha-Tubb Santa Cruz, sc-23950 1:2000 Overnight, RT Citrate buffer, pH 6.0 (Clone number- 6-11B-1)  
 Cytokeratin-8 Santa Cruz, sc-101459 1:50 Overnight, RT Citrate buffer, pH 6.0 (Clone number- Ks8.7)  
 Geminin (Primary Antibody Rabbit, Proteintech Europe, cat. 10802-1-AP)  
 RAD51 (Primary Antibody Mouse, Gene Tex, GTX70230) (Clone number- 14B4)

## Validation

Antibodies were used against human tissue and validated to use by company (Positive and specific IHC staining in human OC tissue (PAX8) Breast cancer tissue (Geminin), positively IF staining in U2OS cells after IR (Rad51)) or previously in our lab (Positive and specific IHC staining in colorectal cancer tissue (Ki67, p53, WT1, CK8), and Lung tissue (Ac-alpha-tubb)).

## Animals and other organisms

Policy information about [studies involving animals](#); [ARRIVE guidelines](#) recommended for reporting animal research

## Laboratory animals

(2210) NOD-Scid IL2Rgnull (Jax) female mice were used for organoid transplantation at the age of 8 weeks

## Wild animals

No wild animals were used

## Field-collected samples

No field-collected samples were used

## Ethics oversight

Experiments on NSG mice were carried out at the Netherlands Cancer Institute according to local and international regulations and ethical guidelines, and were approved by the local and central animal experimental committee at the Netherlands Cancer Institute (AVD3010020172464; IVD 9.1 EGP 8102) 8102)

Note that full information on the approval of the study protocol must also be provided in the manuscript.

## Human research participants

Policy information about [studies involving human research participants](#)

## Population characteristics

OC tissue and blood were obtained from consenting patients who underwent tumor resection and/or drainage of ascites/pleural effusion (n= 33), either before (n=20) or after (neoadjuvant) chemotherapy (n=13). Age(mean+/-SD) 61.6+/-14.8 years. We obtained FT and ovary tissue from women (n=12 and 7, respectively) following pBSO. Age(mean+/-SD) FT- 46.7+/-10.3 years, OSE- 50.3+/-7 years. FT samples were also obtained from 2 donors diagnosed with cervical cancer.

## Recruitment

Relevant patients (diagnosed with either ovarian cancer or designated to go through prophylactic bilateral salpingoophorectomy (pBSO)) were approached. Patients that agreed to take part in this study and signed informed consent form were included. No self selection bias is anticipated.

## Ethics oversight

The collection of patient data and tissue for the generation and distribution of normal FT, OSE and OC organoids, has been performed according to the guidelines of the European Network of Research Ethics Committees (EUREC) following European, national, and local law. The medical ethical committee UMC Utrecht (METC UMCU) approved the biobanking protocol: 14-472 HUB-OVI.

Note that full information on the approval of the study protocol must also be provided in the manuscript.

## Flow Cytometry

### Plots

Confirm that:

- The axis labels state the marker and fluorochrome used (e.g. CD4-FITC).
- The axis scales are clearly visible. Include numbers along axes only for bottom left plot of group (a 'group' is an analysis of identical markers).
- All plots are contour plots with outliers or pseudocolor plots.
- A numerical value for number of cells or percentage (with statistics) is provided.

### Methodology

## Sample preparation

Two-three days after organoids were electroporated with a GFP expressing plasmid they were trypsinized and analyzed

## Instrument

BD FACSAria II flow sorter

## Software

Data was collected using BD FACSDiva and analysed using FlowJo.

## Cell population abundance

No sorting

Gating strategy

Live cells were gated based on forward and side scatter  
About 25% of the cells were GFP positive after gating.  
6 independent experiment were conducted and quantification is presented in Extended Data 6D

Tick this box to confirm that a figure exemplifying the gating strategy is provided in the Supplementary Information.